Available at: https://www.nature.com/articles/s41586-023-06652-x

Dynamic Diagnosis of Metamaterials via Laser-Induced Vibrational Signatures

Yun Kai[1,2], Somayajulu Dhulipala[1,†], Rachel Sun[1,†], Jet Lem[2,3], Washington DeLima[4], Thomas Pezeril[3,5*] & Carlos M. Portela[1,2*]

[1] *Department of Mechanical Engineering, Massachusetts Institute of Technology, Cambridge, MA 02139, USA*
[2] *Institute for Soldier Nanotechnologies, Massachusetts Institute of Technology, Cambridge, MA 02139, USA*
[3] *Department of Chemistry, Massachusetts Institute of Technology, Cambridge, MA 02139, USA*
[4] *Kansas City National Security Campus[‡], Department of Energy, Kansas City, MO 64147, USA*
[5] *Institut de Physique de Rennes, UMR CNRS 6251, Université Rennes, Rennes, France*

[†] *equal contribution*

[‡] *Honeywell Federal Manufacturing & Technologies, LLC manages and operates the Department of Energy's National Security Campus under contract DE- NA- 0002839*

Mechanical metamaterials at the microscale exhibit exotic static properties owing to their engineered building blocks,[1–4] but their dynamic properties have remained significantly less explored. Their design principles can target frequency-dependent properties[5–7] and resilience upon high-strain-rate deformation,[8,9] making them versatile materials for applications in lightweight impact resistance,[10–12] acoustic waveguiding,[7,13] or vibration damping.[14,15] However, accessing dynamic properties at small scales has remained a challenge due to low-throughput and destructive characterization,[8,16,17] or lack of existing testing protocols. Here we demonstrate a high-throughput non-contact framework that employs MHz-wave propagation signatures within a metamaterial to nondestructively extract dynamic linear properties, omnidirectional elastic information, damping properties, and defect quantification. Using rod-like tessellations of microscopic metamaterials, we report up to 94% direction- and rate-dependent dynamic stiffening at strain rates approaching 10^2 s^{-1}, in addition to damping properties 3 times higher than their constituent materials. We also show that frequency shifts in the vibrational response allow for characterization of invisible defects within the metamaterials, and that selective probing allows for construction of experimental elastic surfaces, previously only possible computationally. Our work provides a route for accelerated data-driven discovery of materials and microdevices for dynamic applications such as protective structures, medical ultrasound, or vibration isolation.

Mechanical metamaterials, i.e., materials with functional three-dimensional (3D) morphologies at the micro- or nanoscale, exhibit extraordinary properties dictated by their 3D building blocks. For over a decade, researchers have studied exotic static mechanical properties such as stiffness and strength that approach theoretical limits,[2,18,19] high mechanical resilience or energy absorption,[20–22] or negative Poisson's ratios.[23,24] Despite substantial progress, knowledge of these nano- and microscale metamaterials beyond quasi-static responses has remained limited, motivating explorations in dynamic conditions relevant to high-rate impact mitigation and medical ultrasound where these materials could provide superior performance. Such exotic responses relating to wave propagation[7,13,25], high damping[15,26], or high-rate deformation[11] have been explored theoretically and computationally, but experimental demonstrations have remained scarce. While interest in dynamic properties of metamaterials has outpaced current characterization routes, recent studies have shown promising advancements in some dynamic regimes, from piezo-excitation[6,27] to underwater ultrasound propagation[5], elucidating routes to induce polarization and form band gaps for mechanical waves. However, these pioneering methods have been limited to extracting wave-propagation properties, while extraction of dynamic elastic properties remains challenging. Their contact-based and fluid-coupled measurements pose limitations towards performing high-throughput characterization—a requirement for accelerated progress in understanding metamaterials under dynamic conditions.

Microscale metamaterial properties have historically been extracted from stress-strain curves captured by nanoindentation tools,[1–3,18,19,28] which face a trade-off between deformation amplitude and increases in strain rate. As a result, dynamic mechanical properties of microscale metamaterials[16,29] and full elasticity-tensor approximations[30,31] have only been possible using dynamic numerical frameworks or computational homogenization approaches, respectively. These limitations have left a void in understanding anisotropy, damping properties, and wave propagation in advanced metamaterials. While dynamic characterization techniques at large scales like the split Hopkinson bar method[12,32,33] have served as a proxy to understand microscopic metamaterial behaviour, the contact-based, destructive nature of these methods results in low-throughput, one-time measurements with considerable variability. With advances in data-driven design tools for metamaterials,[31,34,35] experimental throughput has failed to keep up with vast design parameters spaces, particularly in dynamic regimes. A high-throughput method and underlying principles to uncover dynamic responses of metamaterials at small scales could enable characterization and data collection necessary for accelerating design and discovery of new types of metamaterials for various multifunctional applications.

Here, we introduce a framework for characterizing the dynamic response of 3D metamaterials at the microscale, enabled by a non-destructive and non-contact optical framework that converts vibrational signatures to dynamic elastic properties and wave propagation measurements. We demonstrate our high-throughput framework on several morphologies of 3D microscale metamaterials by leveraging pulsed-laser-based photoacoustic excitation[36] of three types of elastic waves within the materials. Given low-amplitude elastic deformation and short timescales of excitation, we employed 10^4 measurements per sample to extract precise damping-property measurements, omnidirectional stiffness, and defect quantification within complex microscale samples. This research paves the way for employing nondestructive vibrational signatures as an alternative to slower microscale contact-based approaches, enabling understanding and discovery of metamaterials in regimes closer to real-world applications.

Laser-induced elastic waves

To enable high-throughput non-destructive characterization of metamaterials at the microscale, we designed a pulsed-laser-based technique to leverage photoacoustic excitation of elastic waves on the surface of the material sample, analogous to photoacoustic thin-film and polycrystalline metal characterization studies[37,38]. Our method—laser-induced resonant acoustic spectroscopy (LIRAS)—is composed of two separate pump and probe modules (Fig. 1a). The pump module consists of a picosecond pulsed laser applied to a three-dimensional sample of interest with a thin chromium coating which partially absorbs the laser pulse and induces broadband acoustic waves (Methods, Extended Data Fig. 1). Resulting sample surface displacements are then measured by the probe module, consisting of a phase-mask interferometer.

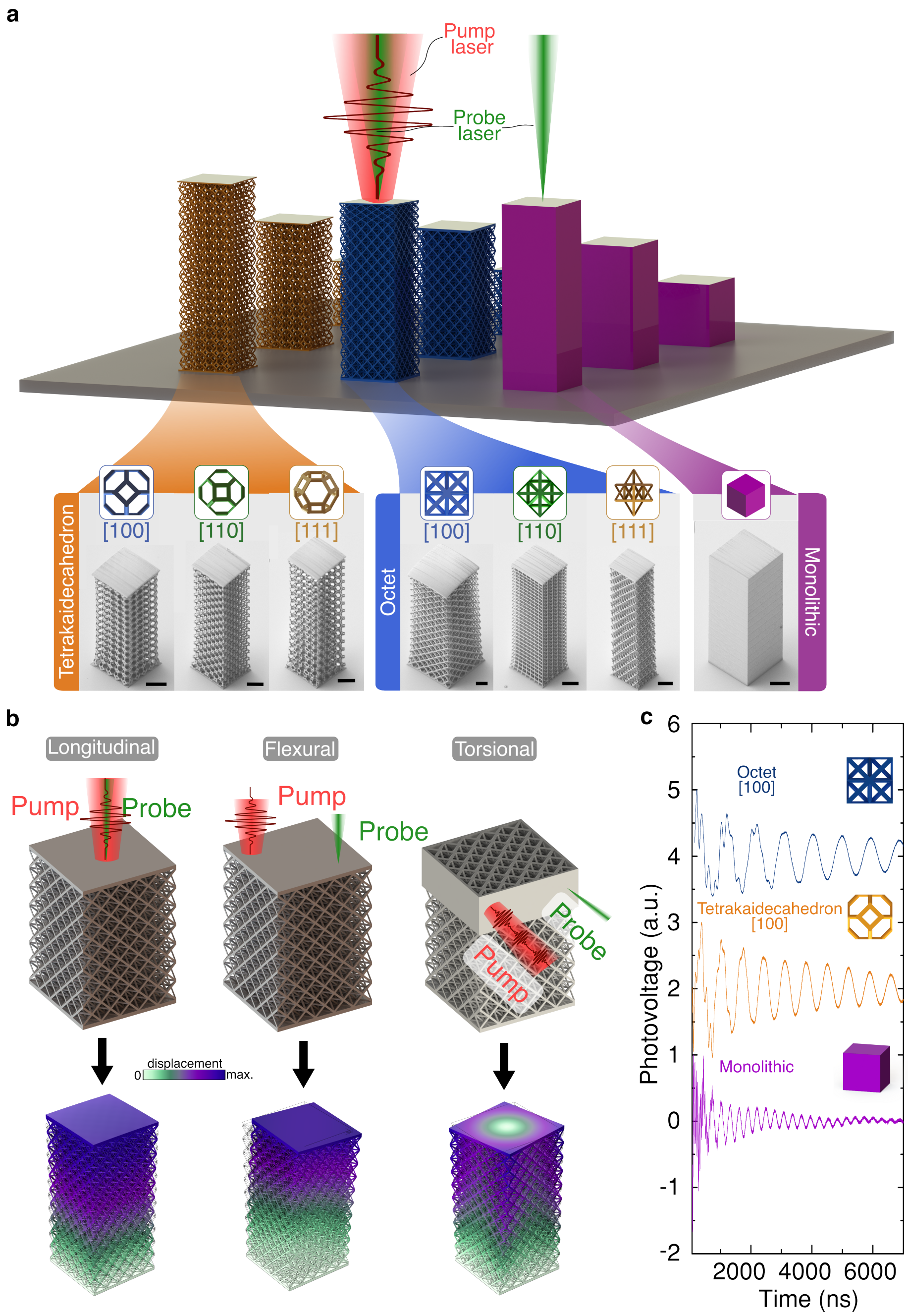

Figure 1 | Non-contact laser-induced excitation and probing of elastic waves in metamaterials. **a**, Schematic of the custom laser-induced resonant acoustic spectroscopy (LIRAS) method, employing a picosecond pump laser and a continuous-wave (CW) laser for interferometry displacement signals. SEM micrographs (insets) depict metamaterial architectures (octet, tetrakaidecahedron, and monolithic) used in our experiments. **b**, Schematic of pump-CW probe schemes to excite longitudinal, torsional, and flexural modes in metamaterials, accompanied by a depiction of resulting resonant modes. **c**, Representative waveforms obtained from longitudinal excitation of octet, tetrakaidecahedron, and monolithic samples. Scale bars in SEM insets, 20 μm.

To facilitate extraction of metamaterial mechanical properties, we fabricated polymeric microlattices out of IP-Dip photoresist in slender aspect ratios using a two-photon lithography system (Nanoscribe GmbH), which approached the limit of rod-like 1D-wave propagation upon excitation (Extended Data Fig. 2). Specifically, we fabricated 5×5×n tessellations of 9.0±0.1 µm octet and tetrakaidecahedron unit cells, with the height of the tessellation n ranging from 4 to 22. Octet and tetrakaidecahedron morphologies were selected as representatives of kinematically rigid and non-rigid architectures, respectively. At relative densities of $\overline{\rho} = 17\%$ for the octet and 14% for the tetrakaidecahedron, these translated to stretching- and bending-dominated mechanical responses[28]. Exploiting cubic symmetry in these classical geometries enabled metamaterial anisotropy detection (insets in Fig. 1a) by fabricating metamaterial samples along lattice orientations such as [100], [110], and [111], and monolithic IP-Dip polymer samples for comparison.

To investigate different types of elastic metamaterial responses, our LIRAS technique enabled excitation and measurement of three types of elastic waves: (i) longitudinal, (ii) torsional, and (iii) flexural waves. Primary excitation of each of these waves was achieved by tuning the pump-continuous-wave (CW) probe scheme of the lasers (Fig. 1b). Specifically, coincident pump-CW probe lasers at the center of the sample induced a primarily longitudinal wave in the metamaterial, while lateral excitation at the top of a modified sample with separate pump-probe locations induced a torsional wave. Similarly, off-center excitation from the top of the sample with different pump-probe sites induced a primarily flexural wave in the metamaterial. As shown in Fig. 1c, characteristic response waveforms attenuated due to inherent vibrational decay but lasted up to ~200 µs depending on sample type and pump scheme (Methods, Extended Data Fig. 3), and experimental calibration enabled translation from photovoltage to surface displacement (Supplementary Information section I).

Metamaterial fabrication onto a glass substrate resulted in clamped and free boundary conditions at the base and top, respectively, inducing standing waves of wavelength $\lambda = 4H/m$ upon laser excitation, where H denotes sample height and m denotes harmonic order (i.e., $m = 1$ indicates the fundamental first harmonic). Consequently, varying sample heights allowed for wavevector $\boldsymbol{k}$ tunability, with the magnitude defined as wavenumber $|\boldsymbol{k}| = 1/\lambda$. Fabricating and testing samples with systematically increasing heights enabled extracting their resonant frequencies for different wavevectors (Fig. 2a).

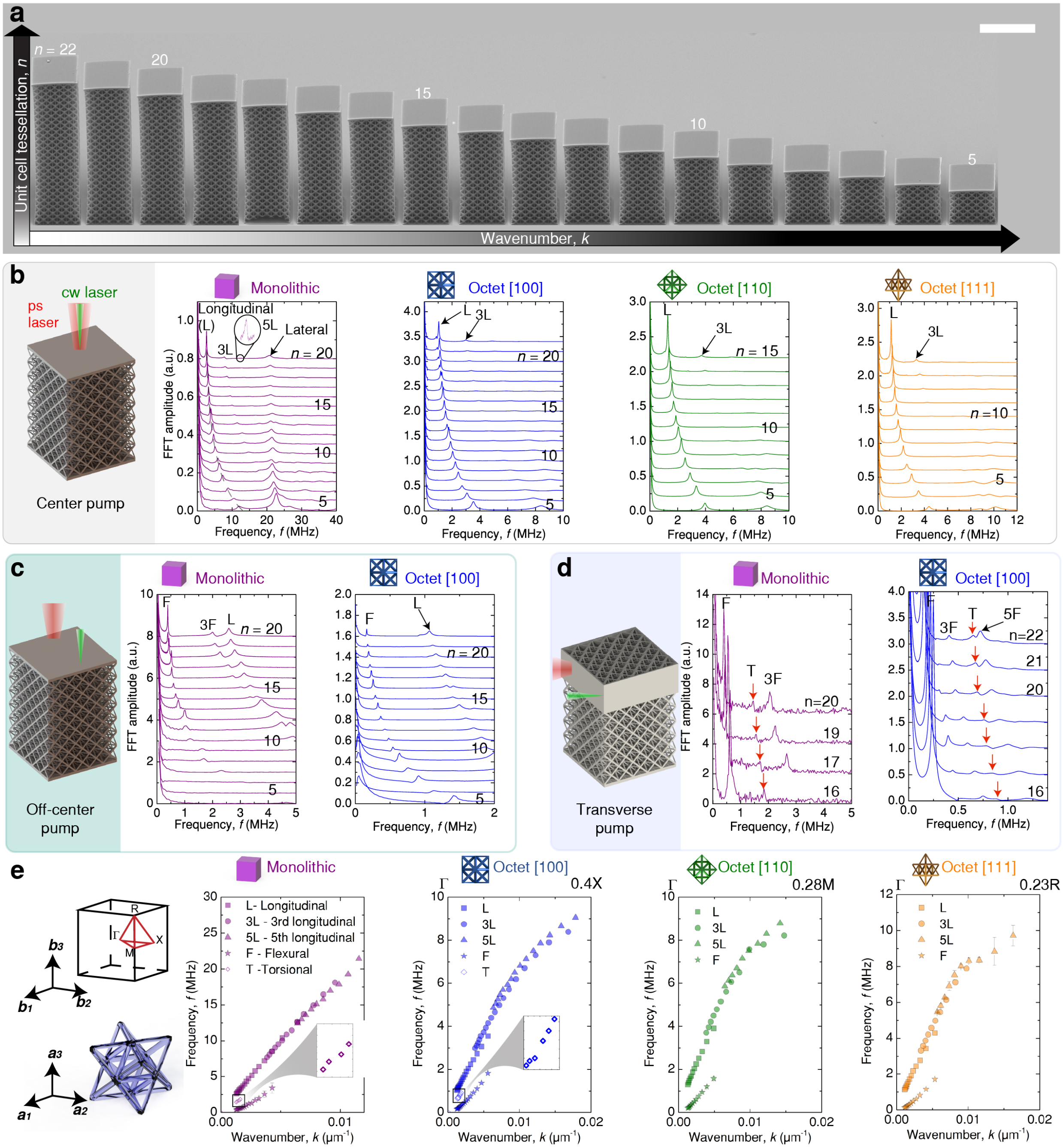

Figure 2 | LIRAS dynamic measurements on metamaterials. **a**, SEM micrographs of selected octet [100] samples of different n tessellations, corresponding to different wavenumbers, scale bar 50 μm. **b**, Fast-Fourier transform (FFT) spectra of detected signals from the surface of the metamaterials using the center pump-CW probe scheme, depicting longitudinal mode (L) and its higher harmonics (e.g., 3L). Spectra corresponding to different n-tessellations are plotted with an offset for illustration purposes. **c**, FFT spectra from off-center scheme, depicting appearance of flexural modes (F) and higher harmonics; and **d**, spectra from the transverse scheme depicting torsional modes (T) and several flexural harmonics. **e**, Dispersion relations $f(\boldsymbol{k})$ extracted from FFT spectra along specific edges of the octet's irreducible Brillouin zone (top left, along with Bravais- and reciprocal-lattice vectors, $\boldsymbol{a}_i$ and $\boldsymbol{b}_i$, respectively).

Following excitation by 10^4 pump-laser pulses per sample (over 1 to <5 minutes, Supplementary Information section II), frequency content of time-domain dynamic responses for the metamaterials was extracted by taking their fast Fourier transform (FFT). Using the center pump-CW probe scheme, we determined the presence of a fundamental longitudinal-mode peak for all $5 \times 5 \times n$ samples (L in monolithic and octet data in Fig. 2b, tetrakaidecahedron in Extended Data Fig. 4). Besides this dominant peak, higher-order harmonics were also measurable for most samples (e.g., 3L and 5L, Fig. 2b). We additionally measured a height-independent Poisson-effect transverse mode in monolithic samples, which was not measurable in metamaterials due to prominent microstructural scattering in this shorter-wavelength regime. Using the off-center pump-CW probe scheme, we primarily excited a flexural mode (and higher-order harmonics) in addition to a weaker longitudinal mode (Fig. 2c). To measure torsional modes, we implemented a transverse pump-CW probe scheme, where metamaterial samples were fabricated with a flat reflective surface on the sides and were pumped and probed at two different transverse locations on that surface (see Fig. 2d). This scheme excited primarily flexural modes, but enabled measurement of a torsional mode. To correlate experimental spectra to corresponding vibrational modes, we confirmed a long-wavelength-limit linear relation between wavenumber and frequency for longitudinal and torsional waves, while a quadratic relation was identified for flexural waves (Extended Data Fig. 5). We further confirmed modal categorization via numerical eigenfrequency analyses on monolithic and metamaterial geometries, which provided qualitative and quantitative agreement for longitudinal, flexural, and torsional modes (Extended Data Figs. 3, 6).

After identifying frequency peaks and their corresponding modes for all samples, each frequency was correlated to a wavenumber based on sample height, enabling construction of experimental dispersion relations for monolithic and metamaterial samples as shown in Fig. 2e (tetrakaidecahedron in Extended Data Fig. 4). Cubic symmetry enabled probing along edges of the irreducible Brillouin zone, corresponding to Γ–X for [100], Γ–M for [110], and Γ–R for [111]. For longitudinal modes in all samples, dispersion was observed for larger wavenumbers, primarily since the samples in this regime violated assumptions for 1D-wave propagation due to their non-slender aspect ratio. Nondispersive longitudinal waves were observed for metamaterial tessellations of $n \geq 10$ when considering only the fundamental mode. Additionally, torsional and flexural waves in monolithic and [100] metamaterial samples were measured, but were excluded in other metamaterial-orientation analyses due to redundancy.

High-throughput dynamic mechanical characterization

While dispersion relations obtained via the LIRAS technique provided insight into different types of elastic waves supported by these metamaterials, we aimed to leverage this information to determine their dynamic mechanical properties. Using measurements in the long-wavelength limit ($|\boldsymbol{k}| \leq 0.0025\ \mu\text{m}^{-1}$, tessellations of $n \geq 10$), we calculated group velocity of each wave type from experimental dispersion relations as $c_g = \frac{\partial f}{\partial k}$. Following theory for 1D-longitudinal-wave propagation in a rod-like medium, we used longitudinal group velocities $c_{g,L}$ to calculate the effective stiffness for each sample as $E^* = \rho c_{g,L}^2$, where ρ is the sample density (Methods). From displacement-calibrated LIRAS experiments, which enabled effective engineering strain measurements ranging from 0.01% to 0.1%, we determined characteristic root mean square (RMS) strain rates of $\dot{\varepsilon} = 38$ s^{-1} for monolithic polymer and $\dot{\varepsilon} = 70$ s^{-1} for octet metamaterials—corresponding to the MHz ultrasound dynamic regime (Methods, Extended Data Fig. 7, Supplementary Information Sections III & IV). As expected for octets and tetrakaidecahedra, measured effective stiffness (Fig. 3a) exhibited direction-dependent values, with [111] and [100] directions yielding the highest stiffness for octet and tetrakaidecahedron samples, respectively.

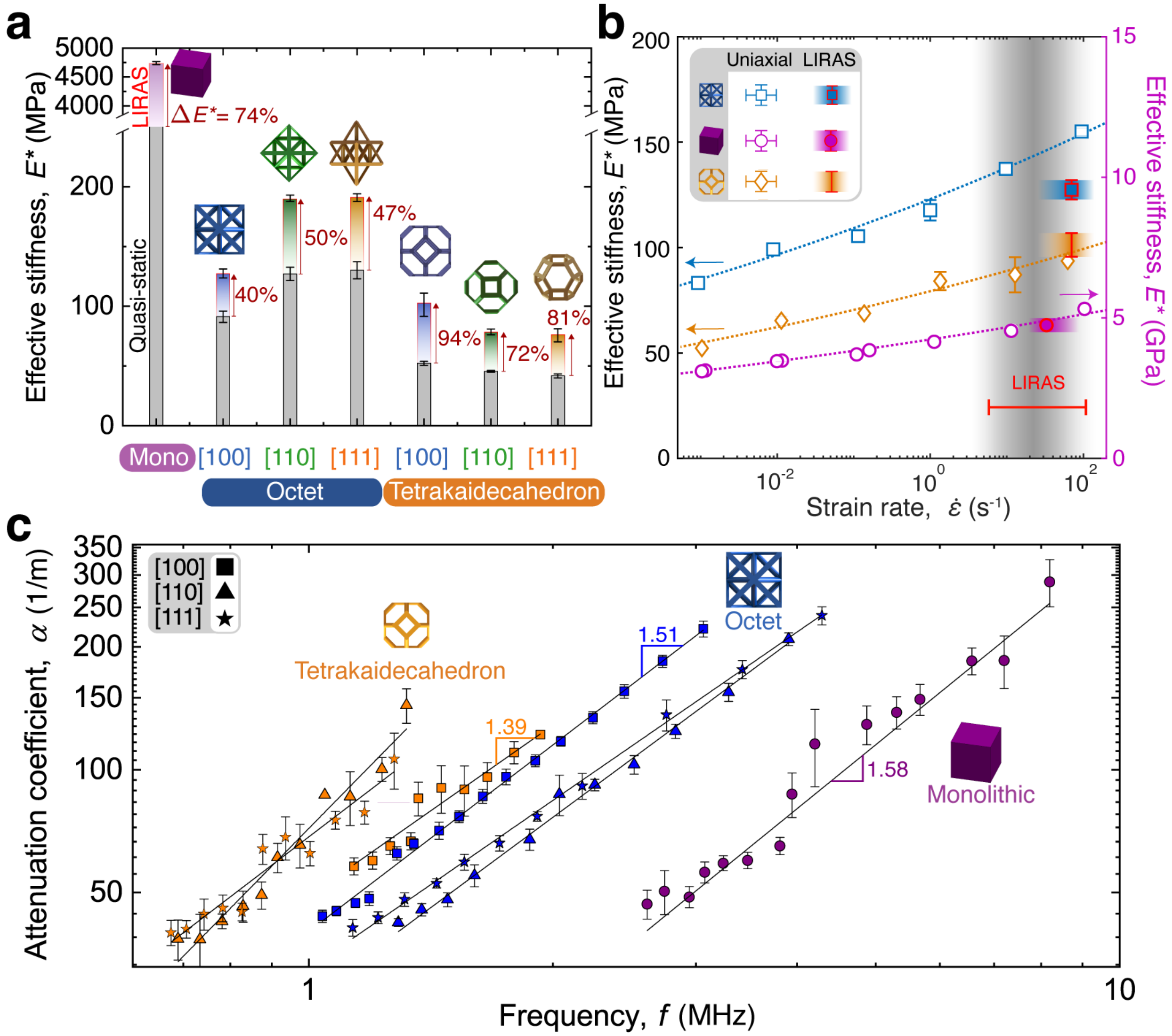

Figure 3 │ Dynamic elastic and damping properties of metamaterials. **a**, LIRAS (color) and quasi-statically obtained (gray, uniaxial compression) effective stiffness E^* depicting dynamic stiffening in samples. **b**, Rate-dependent stiffness of monolithic samples (circular IP-Dip pillars), tetrakaidecahedron, and octet [100] metamaterials depicting agreement of destructive uniaxial compression method with high-throughput LIRAS experiments. **c**, Spatial attenuation coefficient α as a function of frequency f, that follows $\alpha(f) = \beta(f)/c_{p,L}$ [39], where $\beta(f)$ is the temporal damping coefficient and $c_{p,L}$ is the longitudinal phase velocity, depicting higher and anisotropic damping over our measurable frequency range as a power law $\alpha(f) = \alpha_0 f^{\eta}$ with constant a_0 and tunable exponent η ranging from 1.35 to 1.51 (slope of the log-log plot) for octet and 1.39 to 2.02 for tetrakaidecahedron, compared to 1.58 for monolithic polymer.

To quantify dynamic effects on the responses of our samples, we performed quasi-static ($\dot{\varepsilon} = 10^{-3}$ s^{-1}) uniaxial compression experiments using a displacement-controlled nanoindenter (Alemnis AG) on identical samples as those tested via LIRAS (see Extended Data Fig. 7). Comparing the effective stiffness, $E^*(= \partial\sigma/\partial\varepsilon)$, obtained through these two techniques (Fig. 3a) showed dynamic stiffening effects in all samples. From experiments on the monolithic polymer samples, we measured a viscoelastic response in the base material with a dynamic stiffness of 4740 ± 30 MPa, corresponding to a 74% stiffening compared to the measured quasi-static effective Young's modulus, consistent with other dynamic compressions on this material[40]. This stiffening response was also observed in the metamaterial samples, with an on-average stiffening of 46% for the octets and 82% for the tetrakaidecahedra. Despite this direction-dependent dynamic stiffening, the anisotropic response of the metamaterials remained qualitatively unchanged.

Additional uniaxial compression experiments to strain rates of up to 10^2 s^{-1} on both monolithic polymer micropillars and $5 \times 5 \times 5$ tessellations of the [100] octet and tetrakaidecahedron metamaterials (see Methods), confirmed the rate-dependent response observed in LIRAS measurements. Despite the different nature of both characterization techniques, i.e., the contact-based method targets a single strain rate while a range of strain rates are accessed in the free-vibration case, agreement to within 10% was observed across all sample types (Fig. 3b, Supplementary Information Section IV). These measurements confirmed that achieving high-rate nanometer-scale displacements via photoacoustic excitation effectively allows for non-destructive dynamic characterization, presenting an alternative to single-measurement destructive experiments and their concomitant signal-to-noise ratio challenges (see Extended Data Fig. 8).

In addition to enabling high-throughput linear mechanical property measurements, LIRAS frequency-spectrum analysis provided metamaterial damping properties.[15,41] Analogous to a classical damped harmonic oscillator, whose oscillation amplitude is described by $u(t) = u_0 e^{-\beta t} \cos(2\pi f - \delta)$, the exponential temporal decay of the LIRAS experiments from an initial amplitude u_0 at a frequency f and phase shift δ is dictated by the decay parameter β (Supplementary Information Section V). Using center-pump FFT spectra, we calculated the more informative spatial attenuation coefficient[42] $\alpha = \beta/c_{p,L}$ (units m^{-1}), where β scales with the half-width-half-max of the longitudinal peak, and $c_{p,L} = f/|\boldsymbol{k}|$ is phase velocity of the longitudinal waves (Extended Data Fig. 3). Plotting the experimental spatial attenuation coefficient against the dominant longitudinal frequency peak, we measured direction-dependent damping in our metamaterials (Fig. 3c). Specifically, higher damping was observed for the more compliant direction [100] in octets, while the stiffer [110] and [111] directions exhibited an average of 30% lower damping at a frequency of 3 MHz. In tetrakaidecahedra, the compliant [111] direction also exhibited higher damping at a given frequency than its stiffer [100] direction. Remarkably, the octet metamaterials exhibited up to a 3.5× increase in damping ability compared to their constituent monolithic polymer. Fitting spatial attenuation values to the classical frequency-dependent attenuation power law[43] $\alpha(f) = \alpha_0 f^\eta$ yielded a scaling exponent $\eta = 1.51$ (slope in Fig. 3c) for monolithic samples, in alignment with other polymer measurements [44]. In contrast, the metamaterials exhibited direction-dependent scaling, with slopes of 1.51, 1.44, and 1.35 for the octet [100], [110] and [111] directions, respectively, while the tetrakaidecahedron had slopes of 1.39, 2.02, and 1.56 for the same orientations. The measurements indicate that architecture and anisotropy can tune damping properties at a wide range of ultrasonic frequencies. Both metamaterials indicate higher damping capacity in compliant directions and bending-dominated architectures, over stiff and stretching-dominated responses.

Omnidirectional elastic properties

Established characterization methods for metamaterials have primarily been limited to reporting effective Young's moduli only along selected orientations [2,18,28], providing only partial information of material anisotropy and lacking measurement of properties such as effective shear moduli. Numerical methods like computational homogenization have been the preferred technique to obtain full elastic-tensor information of metamaterial geometries, but provide metrics that have not been experimentally validated [21,31,45]. To fill this experimental gap, we harnessed the capabilities of the LIRAS technique to provide fully experimental elastic-tensor extraction for metamaterials under dynamic conditions.

To obtain preliminary validation of properties obtained from LIRAS, pertaining both to the measured frequencies and apparent anisotropy, we employed three computational approaches that together predict expected anisotropy and wave propagation characteristics within the metamaterials. For consistency with the viscoelastic response in the constituent polymer, the material properties used in dynamics simulations corresponded to the RMS strain rate in our experiments, while upper- and lower-bound simulations employed properties corresponding to the maximum strain rate and quasi-static conditions, respectively (Methods, Extended Data Fig. 7, Supplementary Information section IV). The first comparison approach consisted of finite eigenfrequency calculations on a finite-element representation of discrete $5 \times 5 \times n$ tessellations, with boundary conditions identical to those in our LIRAS experiments. Identification of longitudinal, torsional, and flexural resonant modes and associated eigenfrequencies agreed with experimental measurements especially in the long-wavelength limit, as shown in Fig. 4a. As a second validation method, we performed Bloch-wave analysis on metamaterial unit cells, which provided dispersion relations that enabled longitudinal and shear mode identification (Extended Data Fig. 10). Using these two computational methods, we calculated the predicted [100] stiffness for the metamaterials and confirmed an agreement to within 5% when comparing the stiffness from eigenfrequency simulations to the effective stiffness in the LIRAS experiments. The third computational approach consisted of linear static homogenization, which extracted the metamaterials' elasticity tensor $\mathbb{C}$, and enabled calculation of their effective stiffness in all directions[21,28] (Methods) to be represented as an elastic surface (Fig. 4b, top).

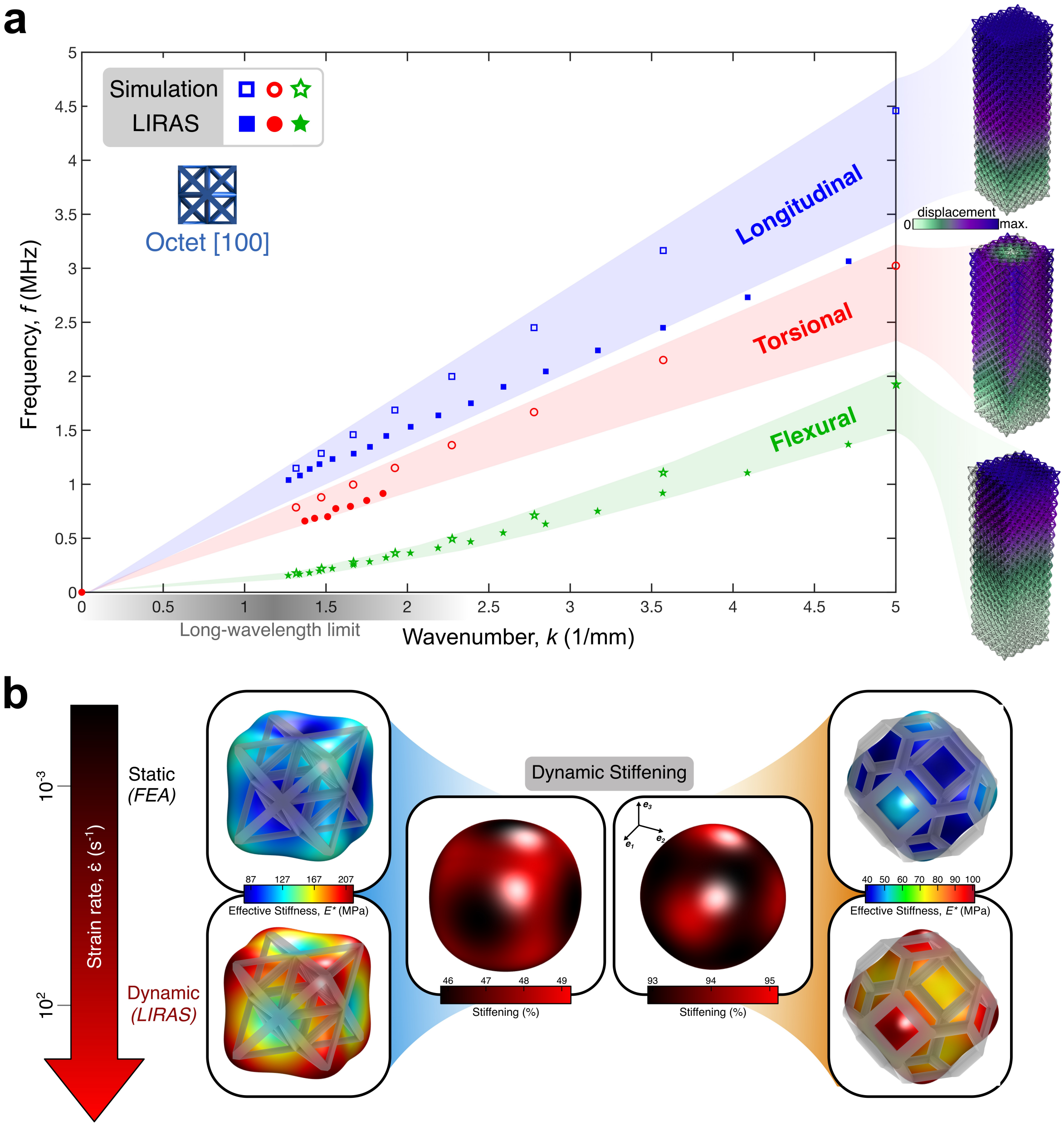

Figure 4 | Wave propagation validation and omnidirectional elastic properties. a, Eigenfrequency analysis (hollow data points) on octet [100] 5×5×*n* tessellations presenting modal and frequency agreement with LIRAS experiments (solid data points). Shaded region depicts upper and lower bounds for material properties, hollow data points correspond to RMS-strain-rate material properties. **b**, Computational static elastic surfaces (top) compared to LIRAS-determined dynamic elastic surfaces (bottom) for the metamaterials, depicting anisotropic and architecture-dependent stiffening (center) under dynamic conditions, calculated as the difference between the static and dynamic surfaces.

After confirming wave propagation response and resulting dynamic stiffness along specific directions, we combined all properties extracted from LIRAS measurements to produce an experimental dynamic elastic surface for our metamaterials (Fig. 4b, Supplementary Information Section VI). Given their cubic symmetry, we used the experimental effective stiffness along the [100], [110], and [111] directions, and the torsional response of the [100] samples, to construct dynamic elasticity and compliance tensors $\hat{\mathbb{C}}$ and $\hat{\mathbb{S}} = \hat{\mathbb{C}}^{-1}$, respectively. Through the relation $\hat{E}_{\boldsymbol{d}} = 1/(\hat{\mathbb{S}}_{ijkl}\boldsymbol{d}_i\boldsymbol{d}_j\boldsymbol{d}_k\boldsymbol{d}_l)$ for a given probing direction $\boldsymbol{d}$, we extracted non-shear components of the compliance tensor $\hat{\mathbb{S}}$. To obtain the shear components, we leveraged torsional waves to relate the torsional wave velocity c_T to the effective dynamic shear stiffness $\hat{G} = \hat{S}_{44}^{-1}$ for these cubic metamaterials via the expression $c_T = K\sqrt{\hat{G}/\rho}$, where K is a constant defined by the cross-section of the body undergoing torsion[46] and ρ again denotes density of the metamaterial (Supplementary Information Section VII). The experimental dynamic elastic surfaces preserved the qualitative anisotropy for the metamaterials, with [111] and [100] remaining as the stiffest directions in the octet and tetrakaidecahedron, respectively, and exhibited dynamic stiffening (Fig. 4b, center) which was computed as the difference between static and dynamic elastic surfaces. Dynamic stiffening for both metamaterials was higher for the stiffest direction, at ~49% and ~95% for the octets and tetrakaidecahedron, respectively. Despite the octet exhibiting omnidirectional stiffening greater than 40%, the tetrakaidecahedron exhibited higher overall dynamic stiffening of 94%, hinting to higher inertial contribution in this bending-dominated architecture (Supplementary Information section VIII).

Non-destructive defect identification

Despite multiple routes to fabricate mechanical metamaterials across scales, various forms of defects emerge from fabrication or processing issues and ultimately degrade their mechanical properties[28,47–49]. At nano-to-microscales, metamaterials still rely on post-fabrication characterization via SEM or 3D X-ray computer tomography (XCT)[18], with inevitable limitations of resolution and time-consuming scans. Other non-destructive techniques employing contact-based ultrasound have been widely employed in structural health monitoring, but they remain inapplicable to small length scales pertinent to metamaterials or microscale electro-mechanical devices.

As an alternative route, we leveraged LIRAS to provide high-throughput defect identification within microscopic samples by measuring changes in their wave propagation response. Specifically, following the center-pump scheme, we identified changes in resonant frequencies as a function of defect density. To validate these capabilities, we studied solid inclusions and missing features, which are common defects in microfabrication techniques such as two-photon lithography[28,47] or larger-scale light-based printing techniques. To mimic solid-inclusion defects commonly caused by unpolymerized resin trapped within the sample, we designed and fabricated 5 × 5 × 10 octet metamaterials with varying degrees of cubic solid inclusions per vertical tessellation layer—undetectable via standard SEM characterization (Fig. 5a). Matching inclusion sizes to those of ~10 μm octet unit cells, we fabricated samples spanning from zero to four defects

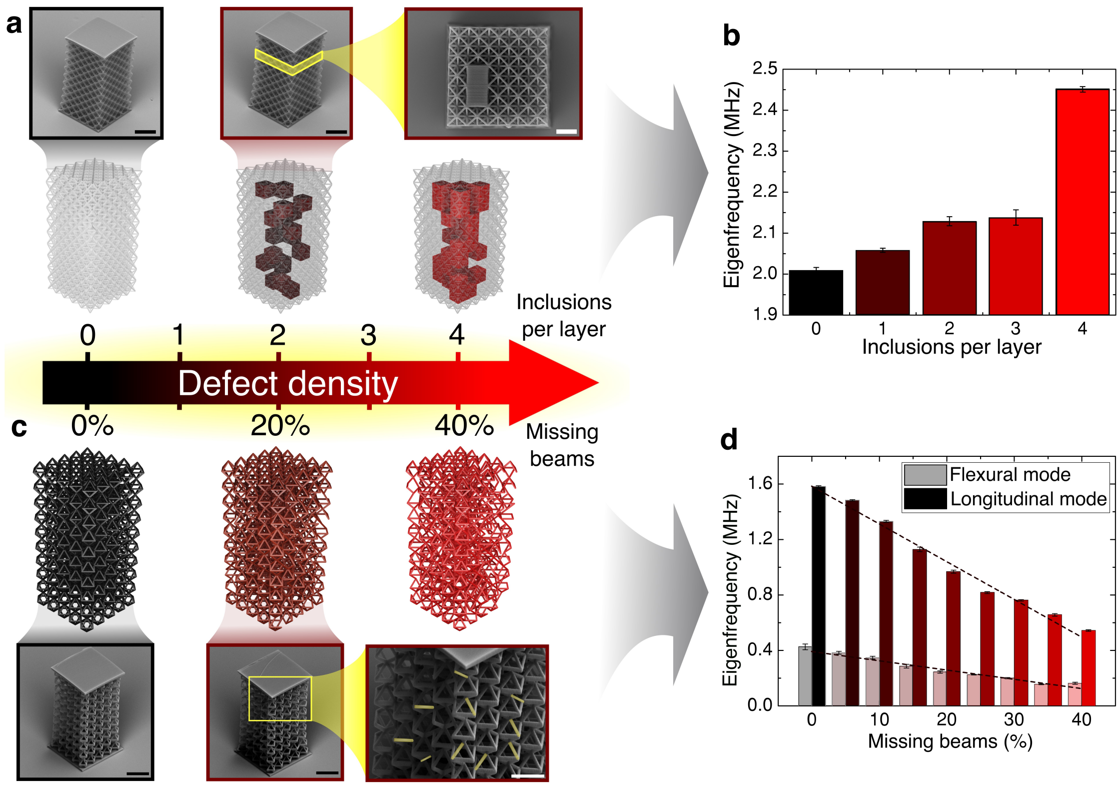

Figure 5 | Vibrational defect identification. **a**, Octet 5 × 5 × 10 metamaterials with internal solid cubic inclusions (CAD and SEM), increasing from 0 to 4 inclusions per n tessellation. **b**, Measured shift in resonant frequencies as a function of inclusion-defect density using the center-pump LIRAS scheme. **c**, Octahedron 5 × 5 × 10 metamaterials with missing beams (CAD and SEM), increasing from 0 to 40% missing features. **d**, Measured shift in longitudinal and flexural resonant frequencies, denoting a linear decrease in frequencies as a function of defect density. Black scale bars, 20 μm; white scale bars, 10 μm.

per layer, measuring their primary resonant mode upon excitation. These experiments identified a ∼2% to 8% increase in resonant frequency when the number of defects per layer ranged from 1 to 3, with respect to an inclusion-free sample (Fig. 5b). A 23% increase in frequency was observed at 4 inclusions per layer, likely due to cumulative solid inclusions resulting in solid domains across several layers which contributed to a significant stiffness increase.

To mimic the second defect type, we designed 5 × 5 × 10 octahedron metamaterials (unit cell size of 10 μm) with intentionally removed beams throughout the tessellation. We selected the octahedron morphology since it retained the octet's stretching-dominated response[28], but its lower beam connectivity enabled easier defect visualization (see Supplementary Information section IX for other morphologies). Starting with a perfect tessellation, we fabricated samples with various percentages of missing beams, with a maximum of 40% missing features to ensure structural integrity (Fig. 5c). LIRAS measurements indicated a gradual decrease in resonant frequency for longitudinal and flexural modes (Fig. 5d, Supplementary Information Section IX). Assuming a linear decrease in longitudinal frequency as a function of missing beams, we identified a 27 kHz decrease per percent of missing beams, compared to a 7 kHz decrease per missing-beam percent for flexural modes. Both defect explorations indicated that a resonant frequency shift provided sufficient resolution to determine defect densities that were otherwise impossible to identify or quantify efficiently.

Summary and Outlook

In summary, we have designed and demonstrated a laser-based framework that enables non-contact high-throughput characterization of microscopic metamaterials. Leveraging elastic wave propagation within the materials, we extracted the full dynamic elasticity tensor and characterized mechanical-wave propagation, damping properties, and quantified the presence of defects. Furthermore, we uncovered the interplay between viscoelastic material properties and 3D architecture, demonstrating direction- and architecture-dependent dynamic stiffening and damping properties. With growing scientific interest in the dynamics of metamaterials, experimental validation to predicted responses is needed, opening the door to high-throughput and non-destructive characterization under extreme conditions.[10] High-throughput characterization techniques (refer to tabular comparison between different techniques in Supplementary Information Section X) in these regimes will also enable rapid creation of experimental datasets for data-driven design, accelerating metamaterial applications in thriving fields relevant to medical ultrasound[50] and nonlinear wave propagation.[25] This framework paves the way for high-throughput discovery of novel nano- and micro-architected materials, on-the-fly defect identification in advanced microscale devices, and microscopic acoustic metamaterial design for medical ultrasound devices.

Methods

Laser-Induced Resonant Acoustic Spectroscopy (LIRAS) method

The pump laser was generated from the uncompressed output of a Ti:Sapphire regenerative amplifier (Coherent Astrella) with a central wavelength of 800 nm, 1 kHz repetition rate, and a pulse duration of 300 ps. A pulse energy of 20 to 50 μJ was applied to induce sudden thermal expansion on the metal-coated (50 nm thick Cr or Au/Pd) sample surface. The probe laser was comprised of a phase mask interferometer driven by a continuous-wave (CW) laser (Coherent Verdi) with 532 nm wavelength and 10 mW maximum output power, while only ~2.5 mW was shone on the sample to avoid damage, monitored by a CCD camera (Hamamatshu Orca C13440). This phase-mask interferometer measured the surface displacement of a given sample as a function of time. Specifically, two CW-laser beams—formed as a result of beam-splitting by the phase mask—were focused on (i) a vibrating sample, and (ii) a static reference sample, respectively (Extended Data Fig. 1). The reflected laser beams from the two samples were recombined by the same phase mask, and the resulting interferometric beam was registered by an avalanche photodetector (c5658, Hamamatsu) with 1 GHz bandwidth and 50 kHz low-frequency cut-off. While vibrating, the sample surface displacement $u_z(t)$ induced an optical path difference $\xi = 2u_z(t)$ between both arms of the interferometer, which was translated into a change of intensity of the signal beam and a measurable change in photovoltage by the photodetector.

Since the pump laser repetition rate was 1 kHz, it excited a resonant vibration 1,000 times per second in a given sample. Consequently, our measurement had a high signal-to-noise ratio attained by averaging of detected waveforms over 10,000 repeated measurements. Due to the acquisition speed in the waveform averaging mode of our oscilloscope (Tektronix TDS 7404), the actual measurement time ranged from 1 to ~3 minutes depending on the signal length and sampling rate.

The interferometric signal $V(t)$ registered by the photodetector was translated to the sample surface displacement $u_z(t)$ by $u_z(t) = \lambda/(4\pi)\sin^{-1}(2V/V_0)$ with $\lambda = 532$ nm as the wavelength of the CW laser and V_0 as the operational range of the photovoltage. Note that the measurement range was limited to a maximum surface displacement of 66.5 nm when the interferometer was operating at the highest sensitivity. However, that range could be extended by tuning the initial phase offset of the interferometer, achieved by a horizontal translation of the phase mask. Because the pump laser induced not only acoustic waves, but also thermal expansion, the surface displacement of the sample showed a combined effect at two different time scales. To eliminate the slow-varying thermal signal (typically μs-periodicity), we fit the displacement waveform with a polynomial function of up to fifth order and subsequently subtracted it from the signal.

Fabrication of polymeric samples

Polymeric samples were fabricated out of IP-Dip resin using a two-photon polymerization system (PPGT2, Nanoscribe GmbH). Octet and tetrakaidecahedron unit cells of nominal dimensions of $10\times10\times10$ μm^3 and strut diameters of 1 μm were the standard metamaterial unit cells. Tessellations of $5\times5\times n$ unit cells, with n ranging from 4 to 22, comprised the rod-like metamaterial samples in this work. Samples were fabricated with a writing speed of ~10 mm s^{-1} and laser power of 30 mW for lattices and 25 mW for monolithic samples. The samples were printed on a glass chip coated with an indium tin oxide (ITO) thin film as the substrate; the coating facilitated better interface finding between the resin and the glass. All samples were developed for 20 min in propylene glycol monomethyl ether acetate (PGMEA), followed by a 5 min. rinse in isopropanol and subsequent drying in a critical point dryer (Autosamdri 931, Tousimis). After fabrication and drying, the chips were coated with 50 nm of Cr by a sputter deposition tool (Orion, AJA International Inc.), yielding a reflective surface for LIRAS excitation. Relative density of each lattice was determined by measuring geometric feature dimensions of each unit cell via scanning electron microscopy (SEM), including unit cell size and strut dimensions, then modeling the unit cell in SolidWorks. The volume of the unit cell was then tabulated and divided by the unit cell bounding-box volume to obtain the relative density. The IP-Dip polymer density was 1170 kg/m^3 (Nanoscribe GmbH), and the relative density for the as-fabricated octet metamaterials was 17 %, yielding 199 kg/m^3 as the effective octet lattice density. The relative density of the as-fabricated tetrakaidecahedron metamaterials was 14%, yielding 162 kg/m^3 as the effective tetrakaidecahedron lattice density.

Fabrication of defect-containing samples

The defect-containing $5 \times 5 \times 10$ samples with bulk inclusions or missing beams were fabricated using the same parameters and process as the octet and tetrakaidecahedron samples. The inclusions were distributed inside the samples, within the inner $3 \times 3 \times 9$ core, such that they were not identifiable via SEM characterization. The missing-beam locations in the octahedron (or braced cubic, Supplementary Information IX) geometries were randomly assigned, resulting in a random distribution of defects within a given sample. A custom code was employed to create missing-beam geometries with various percentages of missing struts, which produced STL files for fabrication via two-photon lithography.

Experimental dispersion relation calculation

The LIRAS voltage-time signals (converted to displacement-time signals via interferometer calibration) were analyzed in MATLAB to remove the thermal background by subtracting the raw data with a fifth-order polynomial fit function (Extended Data Fig. 3). The resulting waveform signal was conditioned with a moving-average filter spanning 5 data points. We extracted the resonant frequencies in the signal by taking the fast Fourier transform (FFT) of the time derivative of the waveform, followed by identification of frequency peaks as shown in Extended Data Fig. 6. The wavenumber for a given peak was calculated as $k = 1/(4H)$ with H denoting the sample height, which was measured via laser confocal microscopy and SEM characterization. Using frequencies extracted from the FFT and calculated wavenumbers from each sample, we constructed partial experimental dispersion relations by plotting frequency f as a function of wavenumber k. To correctly assign each vibration mode to its corresponding dispersion relation, we selectively excited resonant modes and distinguished dispersion trends accordingly. As demonstrated in Fig. 2b–d, a center-pump scheme mainly induced a longitudinal mode, which appeared as the dominant peak in the frequency spectra. Correspondingly, the off-center-pump scheme led to a dominant spectrum peak related to a bending or flexural mode. The transverse-pump scheme excited both flexural and torsional modes. Dispersion analysis[46] was used to distinguish flexural and torsional modes (see Extended Data Fig. 5). Since the fundamental mode was the most dominant peak in the spectra, it was the first to be determined. Subsequently, the expected 3rd and 5th-order harmonics of the modes were calculated by multiplying the measured fundamental frequencies by factors of 3 and 5. All the other measured spectrum peaks were plotted on the same dispersion figure to compare with the higher harmonics of the modes. The modes that matched the expected values were confirmed as higher harmonics. Torsional frequencies were found to be distinctly different to those of other modes.

LIRAS strain rate estimation

Once we obtain the thermal-signal-free time-displacement curves from a LIRAS measurement, dividing by the sample height approximates the effective strain as a function of time $\varepsilon(t)$ (see Supplementary Information Section III). Subsequently, the corresponding strain rates $\dot{\varepsilon}(t)$ can be obtained by taking the time derivative of the strain. The characteristic strain rate for each structure is then calculated by taking the average of the RMS strain rate of the tallest 5 samples (long-wavelength limit). Since free-vibration and subsequent attenuation of the samples encompassed a range of strain rates, the bounds for these ranges were calculated by considering the RMS strain rates for the first and last wavelengths of the signal as shown in Extended Data Fig. 7 and discussed in Supplementary Information Section IV.

Experimental dynamic elastic surface calculation

The directional stiffness was obtained from the longitudinal and torsional wave speeds for 5×5 × n octet and tetrakaidecahedron lattices in different crystallographic orientations. The components of the dynamic compliance tensor, $\hat{\mathbb{S}}_{ijkl}$ were obtained by considering their relation to the effective directional stiffness in prescribed directions (see Supplementary Information Section V). The elastic surface can be computed by calculating the directional stiffness, which for a given direction $\boldsymbol{d}$ is given by $E_{\boldsymbol{d}} = \hat{S}_{ijkl}d_i d_j d_k d_l$.

Damping quantification

The damping coefficients are extracted using only the longitudinal mode due to its strong signal. Using MATLAB to analyze the FFT spectra, we extracted the central frequency of the fundamental longitudinal spectral peak in addition to its full width at half maximum (FWHM), as described in Supplementary Information Section V. Applying a damped harmonic oscillator model to our metamaterial, the FWHM in the frequency domain is related to the decay parameter $\beta(f)$ through $\beta(f)$ =FWHM/2. The spatial attenuation coefficient $\alpha(f)$ can be thus derived from the measured acoustic wave velocities $c_{p,L}$ through $\alpha(f) = \beta(f)/c_{p,L}$. The decay parameter of a classical damped harmonic oscillator can be found by fitting the envelope of the waveform with an exponential function $Ae^{-\beta t}$. However, due to the multi-modal signal with multiple frequency components (Supplementary Information Section V), we elect to perform the damping analysis only in the frequency domain using solely the longitudinal-mode peak.

Quasi-static and dynamic contact-based uniaxial compression experiments

Uniaxial compressions were performed using an Alemnis ASA nanoindenter with a 400 µm-diameter diamond flat-punch tip at strain rates ranging from 10^{-3} s^{-1} (quasi-static) to 10^{2} s^{-1}. Quasi-static experiments were performed on IP-Dip pillars (162.8 µm tall and 50 µm-wide square cross-section) and 5×5×10 octet and tetrakaidecahedron [100], [110], and [111] lattices. The IP-Dip pillars and octet lattices were printed on a silicon substrate using two-photon polymerization at a laser power of 22.5 mW and 30 mW, respectively. A standard load cell with a load range of 2.5 N and a piezostack with a displacement range of 100 µm were used for compression. The tip was operated in a displacement-controlled mode. The high-strain-rate experiments were performed on IP-Dip pillars (diameter of 21.9 µm, height of 43.3 µm) and 5×5×5 octet and tetrakaidecahedron [100] lattices (for consistency, these samples were also compressed at a quasi-static strain rate of 10^{-3} s^{-1}). For high-rate compressions, we employed the Alemnis high strain rate (HSR) module, comprised of a mini load cell (MLC) connected to a signal amplifier. Displacement rates from 50 nm/s to 5 mm/s were applied while maintaining close to 2×10^{3} points for sampling the data at all strain rates. The displacement rates were set by assuming a constant sensitivity (the ratio of the change in displacement to the change in voltage of the piezo stack) determined through an air indent and then setting up a voltage ramp with smoothing. For strain rates of 10^{-3} and 10^{-2} s^{-1}, a maximum displacement of 10 µm was applied. For a strain rate of 10^{0} s^{-1}, a displacement of 30 µm was applied and the samples were compressed in the last 15 µm of the compression. This procedure ensured that the indenter tip accelerated and reached a constant displacement rate before coming in contact with the sample. Similarly for strain rates above 10^0 s^{-1}, a total displacement of 80 μm was applied with the sample coming in contact in the last 40% of the displacement range. The effective stiffness of the samples was measured by calculating the slope of a least-squares linear fit to the linear loading region of the stress-strain data. The strain range for the linear fit was restricted to 3% strain—well within the yield point of the samples. The strain rate for the samples was determined by measuring the total change in strain over the range of the linear fit for the stiffness and dividing that by the time taken for the change in strain. These are all found to be within 5% of the strain rate set for each study.

Computational Analysis

Dynamic explicit simulations

We conducted dynamic explicit simulations in ABAQUS/Explicit on an octet and tetrakaidecahedron unit cells with unit cell size of 7.5 mm and relative densities of 14% and 17% respectively. The unit cells were meshed with C3D10M elements. The compression was enforced with top and bottom planes tied and coupled kinematically to the top and bottom of the unit cell, respectively. The top plate was set to compress such that a maximum 5% engineering strain was enforced at a 60 s^{-1} strain rate with general contact properties, and an encastre boundary condition for all degrees of freedom on the bottom plate. Material properties were set such that Young's modulus of the constituent material was 2.7 GPa, density was 1,200 $\mathrm{kg/m}^3$, and Poisson's ratio was 0.49.

Eigenfrequency analysis

We conducted the eigenfrequency simulations using the solid mechanics module in COMSOL. As in the experiments, the bottom of each metamaterial sample was fixed while all other parts were free to vibrate. The modeled geometry reflected measured values of fabricated samples, with octet unit cell sizes of 9 μm and strut radius of 0.58 μm. The models output the eigenfrequency f corresponding to each vibration mode for different sample heights, i.e., different wavenumbers k. Thereby, we constructed a simulated acoustic dispersion relation $f(k)$ for finite lattice tessellations of a cross-section of 5×5 unit cells in x and y directions with varying numbers of unit cells in the z direction. Monolithic samples were also simulated with a similar aspect ratios, with a fixed cross-section of 50 μm by 50 μm with different heights such that a rod-wave approximation was achieved (Extended Data Fig. 2). Since different strain-rate compressions of monolithic samples confirmed a rate-dependent stiffness of the IP-Dip polymer, the scaling was determined to be $E^* = 4.216\,\dot{\varepsilon}^{0.0445}$ GPa. The strain rate $\dot{\varepsilon}$ was estimated via the method described in Extended Data Fig. 9. We simulated lower, middle, and upper eigenfrequencies by simulating with Young's moduli corresponding to the quasi-static effective Young's Modulus of 2.7 GPa, mean RMS dynamic effective stiffness of 4.522 GPa (strain rate of 4.84 s^{-1}), and maximum dynamic effective stiffness of 5.168 GPa (strain rate of 97 s^{-1}), respectively. Other material properties were held constant with Poisson's ratio of 0.49 and density of 1,170 $\mathrm{kg/m}^3$. Mesh size was determined by keeping a constant maximum and minimum element size, leading to $\sim 85,000$ tetrahedral elements per tessellation layer, as this was the finest possible mesh size due to computational constraints.

Bloch-wave analysis

In addition to the eigenfrequency simulation, we applied Bloch-wave analysis within a finite element method framework to obtain a dispersion relation for octet lattices (Extended Data Fig. 10). We simulated Bloch-wave analysis with experimental geometric values of octet unit cell size 9 µm, elliptical strut width of 0.9 µm, elliptical strut height of 1.96 µm, and material properties of Young's modulus of 4.522 GPa (corresponding to strain rate of 4.84 1/s), Poisson's ratio of 0.49, and density of 1170 kg/m^3. We used Floquet-Bloch periodic boundary conditions in the COMSOL Solid Mechanics module, using symmetric fine physics-controlled mesh. We extracted the first three modes corresponding to the lowest longitudinal and two transverse waves of the lattice structure and calculated a best fit using least-squares regression to extract the longitudinal and shear wave velocities, which were used to populate the stiffness tensor; we then obtained Young's modulus and shear modulus from the compliance tensor [45]. We used volume-averaged modal displacement along principal directions to identify the mode shapes.

Static homogenization

To obtain the directional stiffness, computational homogenization for the octet and tetrakaidecahedron morphologies was performed on ABAQUS/Standard (Simulia). Octet and tetrakaidecahedron unit cells were built using the ABAQUS CAD module and meshed with quadratic tetrahedral (C3D10) elements with full integration. A Young's Modulus of 2.7 GPa and a Poisson's ratio of 0.49 were used for the simulations. A mesh-convergence study was performed to give a final mesh size of 38,660 elements and 152,682 elements for the octet and tetrakaidecahedron unit cell meshes, respectively. Periodic Boundary Conditions (PBC)[21] were applied such that the relative displacement between opposite faces was constrained and an average strain was imposed on the unit cell. Linear perturbation was performed on the unit cells for 6 linearly independent strain vectors. The corresponding stresses for the applied strains were obtained and the compliance tensor $\hat{\mathbb{S}}$ was constructed from these.

References Cited

1. Meza, L. R., Das, S. & Greer, J. R. Strong, lightweight, and recoverable three-dimensional ceramic nanolattices. *Science* **345**, 1322–1326 (2014). URL `http://www.sciencemag.org/cgi/doi/10.1126/science.1255908`.

2. Zheng, X. *et al.* Ultralight, ultrastiff mechanical metamaterials. *Science* **344**, 1373–1377 (2014). URL `http://www.sciencemag.org/cgi/doi/10.1126/science.1252291`.

3. Tancogne-Dejean, T., Diamantopoulou, M., Gorji, M. B., Bonatti, C. & Mohr, D. 3D Plate-Lattices: An Emerging Class of Low-Density Metamaterial Exhibiting Optimal Isotropic Stiffness. *Advanced Materials* **30**, 1803334 (2018). URL `http://doi.wiley.com/10.1002/adma.201803334`.

4. Berger, J. B., Wadley, H. N. & McMeeking, R. M. Mechanical metamaterials at the theoretical limit of isotropic elastic stiffness. *Nature* **543**, 533–537 (2017). URL `http://dx.doi.org/10.1038/nature21075`. `NIHMS150003`.

5. Krödel, S. & Daraio, C. Microlattice Metamaterials for Tailoring Ultrasonic Transmission with Elastoacoustic Hybridization. *Physical Review Applied* **6**, 064005 (2016). URL `http://link.aps.org/doi/10.1103/PhysRevApplied.6.064005`.

6. Frenzel, T., Köpfler, J., Jung, E., Kadic, M. & Wegener, M. Ultrasound experiments on acoustical activity in chiral mechanical metamaterials. *Nature Communications* **10**, 3384 (2019). URL `http://www.nature.com/articles/s41467-019-11366-8`.

7. Bayat, A. & Gaitanaros, S. Wave Directionality in Three-Dimensional Periodic Lattices. *Journal of Applied Mechanics* **85**, 011004 (2017). URL `http://appliedmechanics.asmedigitalcollection.asme.org/article.aspx?doi=10.1115/1.4038287`.

8. Portela, C. M. *et al.* Supersonic impact resilience of nanoarchitected carbon. *Nature Materials* **20**, 1491–1497 (2021). URL `http://dx.doi.org/10.1038/s41563-021-01033-zhttp://www.nature.com/articles/s41563-021-01033-zhttps://www.nature.com/articles/s41563-021-01033-z`.

9. Lai, C. Q. & Daraio, C. Highly porous microlattices as ultrathin and efficient impact absorbers. *International Journal of Impact Engineering* **120**, 138–149 (2018). URL `https://doi.org/10.1016/j.ijimpeng.2018.05.014https://linkinghub.elsevier.com/retrieve/pii/S0734743X17311223`.

10. Dattelbaum, D. M., Ionita, A., Patterson, B. M., Branch, B. A. & Kuettner, L. Shock-wave dissipation by interface-dominated porous structures. *AIP Advances* **10**, 075016 (2020). URL `https://doi.org/10.1063/5.0015179http://aip.scitation.org/doi/10.1063/5.0015179`.

11. Mueller, J., Matlack, K. H., Shea, K. & Daraio, C. Energy Absorption Properties of Periodic and Stochastic 3D Lattice Materials. *Advanced Theory and Simulations* **2**, 1900081 (2019). URL `https://onlinelibrary.wiley.com/doi/abs/10.1002/adts.201900081`.

12. Weeks, J. S. & Ravichandran, G. High strain-rate compression behavior of polymeric rod and plate Kelvin lattice structures. *Mechanics of Materials* **166**, 104216 (2022). URL `https://linkinghub.elsevier.com/retrieve/pii/S0167663622000059`.

13. Guo, Y. *et al.* Minimal Surface-Based Materials for Topological Elastic Wave Guiding. *Advanced Functional Materials* **32** (2022).

14. Matlack, K. H., Bauhofer, A., Krödel, S., Palermo, A. & Daraio, C. Composite 3D-printed metastructures for low-frequency and broadband vibration absorption. *Proceedings of the National Academy of Sciences* **113**, 8386–8390 (2016). URL `http://arxiv.org/abs/1511.09465%0Ahttp://dx.doi.org/10.1073/pnas.1600171113http://www.pnas.org/lookup/doi/10.1073/pnas.1600171113`. `1511.09465`.

15. Hussein, M. I. & Frazier, M. J. Metadamping: An emergent phenomenon in dissipative metamaterials. *Journal of Sound and Vibration* **332**, 4767–4774 (2013).

16. Hawreliak, J. A. *et al.* Dynamic Behavior of Engineered Lattice Materials. *Scientific Reports* **6**, 28094 (2016). URL `http://www.nature.com/articles/srep28094`.

17. Lind, J., Robinson, A. K. & Kumar, M. Insight into the coordinated jetting behavior in periodic lattice structures under dynamic compression. *Journal of Applied Physics* **128** (2020).

18. Crook, C. *et al.* Plate-nanolattices at the theoretical limit of stiffness and strength. *Nature Communications* **11**, 1579 (2020). URL `http://dx.doi.org/10.1038/s41467-020-15434-2http://www.nature.com/articles/s41467-020-15434-2`.

19. Bauer, J., Schroer, A., Schwaiger, R. & Kraft, O. Approaching theoretical strength in glassy carbon nanolattices. *Nature Materials* **8** (2016).

20. Meza, L. R. *et al.* Resilient 3D hierarchical architected metamaterials. *Proceedings of the National Academy of Sciences of the United States of America* **112**, 11502–7 (2015). URL `http://www.pnas.org/content/112/37/11502.abstract`.

21. Portela, C. M. *et al.* Extreme mechanical resilience of self-assembled nanolabyrinthine materials. *Proceedings of the National Academy of Sciences* **117**, 5686–5693 (2020). URL `http://www.pnas.org/lookup/doi/10.1073/pnas.1916817117https://pnas.org/doi/full/10.1073/pnas.1916817117`.

22. Guell Izard, A., Bauer, J., Crook, C., Turlo, V. & Valdevit, L. Ultrahigh Energy Absorption Multifunctional Spinodal Nanoarchitectures. *Small* **15**, 1–8 (2019).

23. Babaee, S. *et al.* 3D soft metamaterials with negative poisson's ratio. *Advanced Materials* **25**, 5044–5049 (2013).

24. Farzaneh, A., Pawar, N., Portela, C. M. & Hopkins, J. B. Sequential metamaterials with alternating Poisson's ratios. *Nature Communications* **13**, 1041 (2022). URL `https://www.nature.com/articles/s41467-022-28696-9`.

25. Jin, L. *et al.* Guided transition waves in multistable mechanical metamaterials. *Proceedings of the National Academy of Sciences of the United States of America* **117**, 2319–2325 (2020).

26. Baravelli, E. & Ruzzene, M. Internally resonating lattices for bandgap generation and low-frequency vibration control. *Journal of Sound and Vibration* **332**, 6562–6579 (2013). URL `http://dx.doi.org/10.1016/j.jsv.2013.08.014`.

27. Iglesias Martínez, J. A. *et al.* Experimental observation of roton-like dispersion relations in metamaterials. *Science Advances* **7** (2021). URL `https://www.science.org/doi/10.1126/sciadv.abm2189`.

28. Meza, L. R. *et al.* Reexamining the mechanical property space of three-dimensional lattice architectures. *Acta Materialia* **140**, 424–432 (2017). URL `http://dx.doi.org/10.1016/j.actamat.2017.08.052https://linkinghub.elsevier.com/retrieve/pii/S1359645417307073`.

29. Lind, J., Jensen, B. J., Barham, M. & Kumar, M. In situ dynamic compression wave behavior in additively manufactured lattice materials. *Journal of Materials Research* **34**, 2–19 (2019).

30. Deshpande, V. S., Fleck, N. A. & Ashby, M. F. Effective properties of the octet-truss lattice material. *Journal of the Mechanics and Physics of Solids* **49**, 1747–1769 (2001).

31. Bastek, J.-H., Kumar, S., Telgen, B., Glaesener, R. N. & Kochmann, D. M. Inverting the structure–property map of truss metamaterials by deep learning. *Proceedings of the National Academy of Sciences* **119** (2022). URL `https://pnas.org/doi/full/10.1073/pnas.2111505119`.

32. Weeks, J. S., Gandhi, V. & Ravichandran, G. Shock compression behavior of stainless steel 316L octet-truss lattice structures. *International Journal of Impact Engineering* **169**, 104324 (2022). URL `https://doi.org/10.1016/j.ijimpeng.2022.104324https://linkinghub.elsevier.com/retrieve/pii/S0734743X22001671`.

33. Tancogne-Dejean, T., Spierings, A. B. & Mohr, D. Additively-manufactured metallic micro-lattice materials for high specific energy absorption under static and dynamic loading. *Acta Materialia* **116**, 14–28 (2016). URL `http://linkinghub.elsevier.com/retrieve/pii/S1359645416304153`.

34. Gongora, A. E. *et al.* Designing lattices for impact protection using transfer learning. *Matter* **5**, 2829–2846 (2022).

35. Mao, Y., He, Q. & Zhao, X. Designing complex architectured materials with generative adversarial networks. *Science Advances* **6** (2020).

36. Abi Ghanem, M. *et al.* Longitudinal eigenvibration of multilayer colloidal crystals and the effect of nanoscale contact bridges. *Nanoscale* **11**, 5655–5665 (2019).

37. Akimov, A., Young, E., Sharp, J., Gusev, V. & Kent, A. Coherent hypersonic closed-pipe organ like modes in supported polymer films. *Applied Physics Letters* **99**, 021912 (2011).

38. Dryburgh, P. *et al.* Measurement of the single crystal elasticity matrix of polycrystalline materials. *Acta Materialia* **225** (2022).

39. Garrett, S. L. *Understanding Acoustics: An Experimentalist's View of Sound and Vibration* (Springer Nature, 2020).

40. Rohbeck, N. *et al.* Effect of high strain rates and temperature on the micromechanical properties of 3D-printed polymer structures made by two-photon lithography. *Materials and Design* **195**, 1–9 (2020).

41. Salari-Sharif, L. *et al.* Damping of selectively bonded 3D woven lattice materials. *Scientific Reports* **8**, 6–11 (2018). URL `http://dx.doi.org/10.1038/s41598-018-32625-6`.

42. Pouet, B. F. & Rasolofosaon, N. J. P. Measurement of broadband intrinsic ultrasonic attenuation and dispersion in solids with laser techniques. *The Journal of the Acoustical Society of America* **93**, 1286–1292 (1993). URL `http://asa.scitation.org/doi/10.1121/1.405413`.

43. Szabo, T. L. Time domain wave equations for lossy media obeying a frequency power law. *The Journal of the Acoustical Society of America* **96**, 491–500 (1994). URL `http://asa.scitation.org/doi/10.1121/1.410434`.

44. Szabo, T. L. & Wu, J. A model for longitudinal and shear wave propagation in viscoelastic media. *The Journal of the Acoustical Society of America* **107**, 2437–2446 (2000). URL `http://asa.scitation.org/doi/10.1121/1.428630`.

45. Patil, G. U. & Matlack, K. H. Effective property evaluation and analysis of three-dimensional periodic lattices and composites through Bloch-wave homogenization. *The Journal of the Acoustical Society of America* **145**, 1259–1269 (2019). URL `http://asa.scitation.org/doi/10.1121/1.5091690`.

46. Graff, K. F. *Wave Motion in Elastic Solids*. Dover Books on Physics (Dover Publications, 2012). URL `https://books.google.com/books?id=jorRAgAAQBAJ`.

47. Gross, A., Pantidis, P., Bertoldi, K. & Gerasimidis, S. Correlation between topology and elastic properties of imperfect truss-lattice materials. *Journal of the Mechanics and Physics of Solids* **124**, 577–598 (2019). URL `https://linkinghub.elsevier.com/retrieve/pii/S0022509618308615`.

48. Liu, L., Kamm, P., García-Moreno, F., Banhart, J. & Pasini, D. Elastic and failure response of imperfect three-dimensional metallic lattices: the role of geometric defects induced by Selective Laser Melting. *Journal of the Mechanics and Physics of Solids* **107**, 160–184 (2017). URL `http://dx.doi.org/10.1016/j.jmps.2017.07.003`.

49. Glaesener, R. *et al.* Predicting the influence of geometric imperfections on the mechanical response of 2D and 3D periodic trusses. *Acta Materialia* **254**, 118918 (2023). URL `https://www.sciencedirect.com/science/article/pii/S1359645423002495https://linkinghub.elsevier.com/retrieve/pii/S1359645423002495`.

50. Wang, C. *et al.* Bioadhesive ultrasound for long-term continuous imaging of diverse organs. *Science* **377**, 517–523 (2022). URL `https://www.science.org/doi/10.1126/science.abo2542`.

Acknowledgements We acknowledge financial support from KCNSC (PDRD# 705288). C.M.P. acknowledges support from the National Science Foundation (NSF) CAREER Award [CMMI-2142460], partial support from DEVCOM ARL Army Research Office through the MIT Institute for Soldier Nanotechnologies (ISN) under Cooperative Agreement number W911NF-23-2-0121, and the MIT MechE MathWorks Seed Fund. This work was carried out in part through the use of MIT.nano's facilities. The authors thank A. Maznev, D.W. Yee, and K.A. Nelson for helpful discussions, T. Butruille for experimental support, R. Glaesener for imperfect-lattice design, and B. Aymon for explicit dynamics simulation support.

Author Contributions Y.K., T.P. and C.M.P. designed the research. Y.K. and C.M.P. designed the samples. Y.K. J.L., and T.P. conducted the LIRAS experiments. S.D. performed the elastic surface calculations. R.S. and S.D. performed the nanomechanical experiments. R.S., Y.K., and C.M.P. performed the acoustic finite element calculations. Y.K., T.P., W.D., and C.M.P. interpreted the results. Y.K., S.D., R.S., and C.M.P. wrote the manuscript with input from all authors.

Supplementary information is appended to the end of this document.

Competing interests The authors declare that they have no competing financial interests.

Data Availability The data sets generated during and/or analysed during the current study are available within the main text or Supplementary Information.

Correspondence Correspondence should be addressed to C.M.P. or T.P.
(emails: cportela@mit.edu, pezeril@mit.edu).

Extended Data Figures

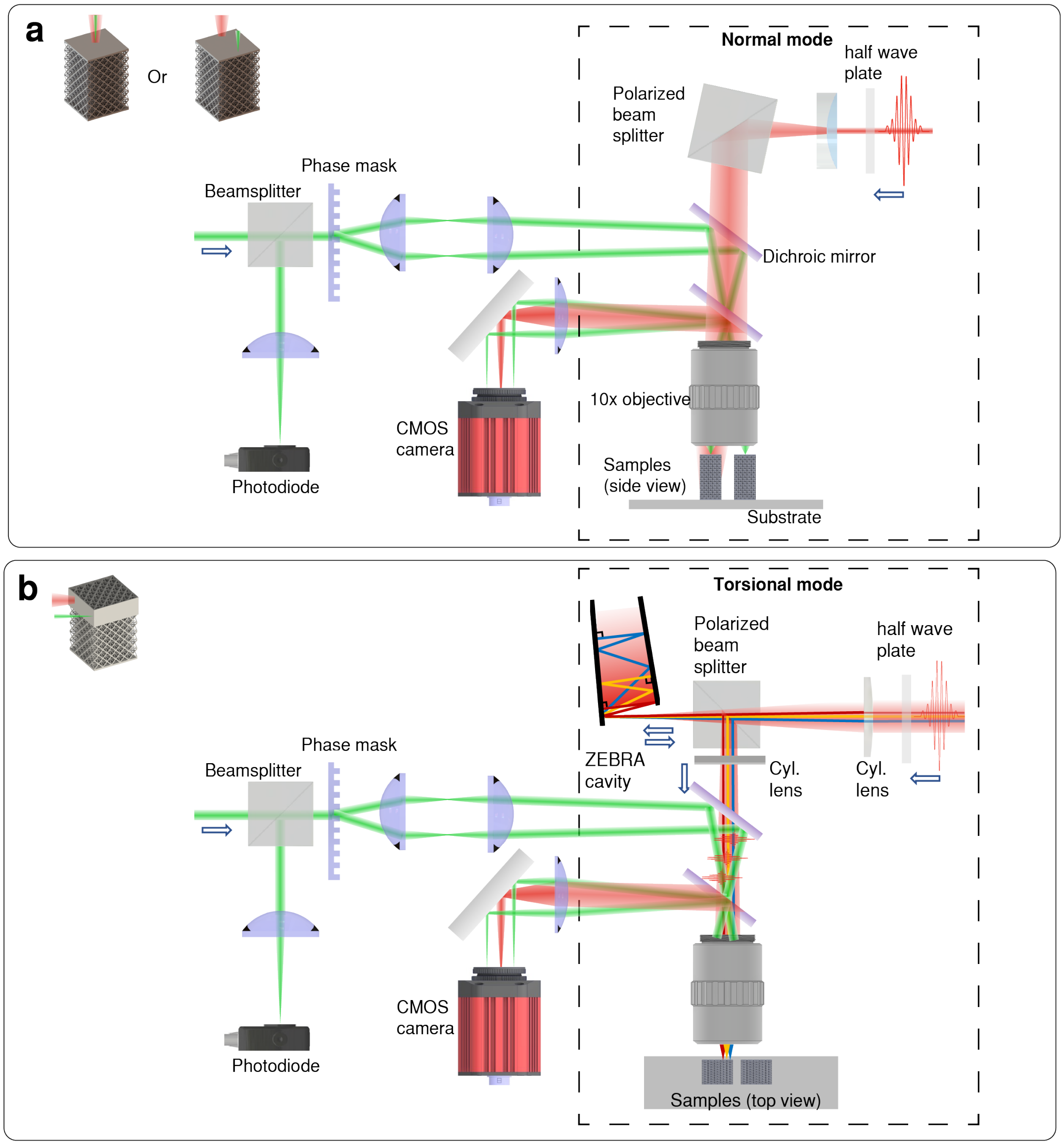

Extended Data Figure 1 | LIRAS setup schematics. The red beam indicates the picosecond laser serving as the pump laser, and the green beams indicate the continuous-wave (CW) laser as the probe laser. The CMOS camera serves to monitor the samples. The interferometric signal corresponding to the waveforms of the sample-surface displacement are registered by an avalanche photodiode. The dashed boxes indicate variations of the LIRAS setup for the selective excitation of **a**, longitudinal & flexural, and **b**, torsional modes.

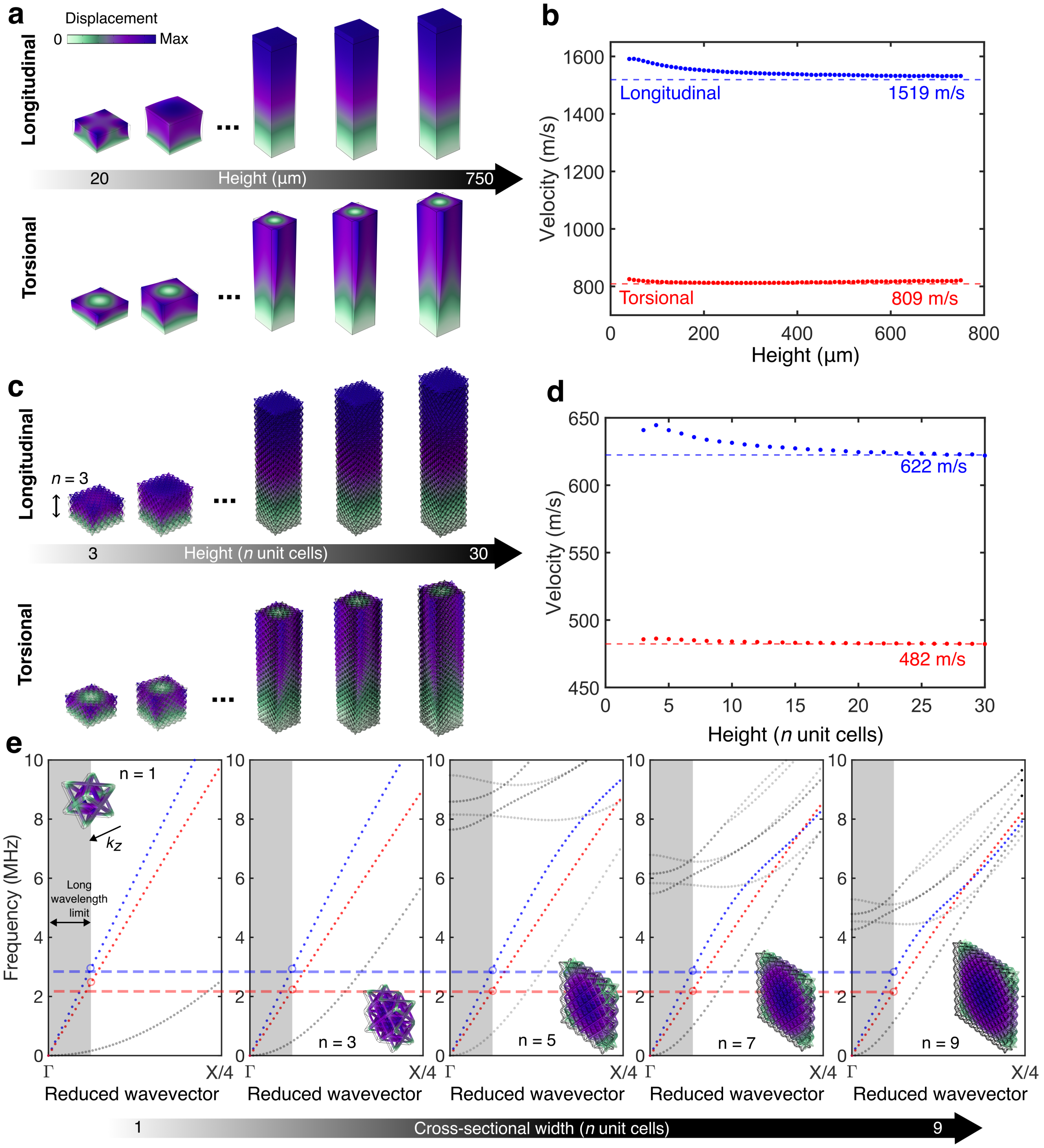

Extended Data Figure 2 │ Eigenfrequency studies to validate rod-wave approximations. **a**, Eigenfrequency analysis of monolithic Ip-Dip pillars (density 1170 kg/m^3, Young's modulus 2.7 GPa, and Poisson's ratio 0.49) of different aspect ratios; **b**, corresponding computed wave velocities. **c**, Computation of octet eigenfrequencies of different heights with a fixed cross-section of 50 µm × 50 µm (i.e., a 5×5 tessellation); **d**, corresponding computed wave velocities. While no clear longitudinal mode could be identified for short samples with heights ≤ 20 µm, taller samples asymptotically approached the theoretical rod-wave-velocity value (dashed lines in b and d). **e**, Bloch-wave analyses on $n \times n \times \infty$ tessellations (∞ tessellation in the z-direction stems from Bloch-Floquet periodic boundary conditions) yield dispersion relations as a function of wave vector k_z for each of these $n \times n$ cross-sections. Longitudinal and transverse bands for tessellations ranging from $n = 5$ to 9 are in agreement within the long-wavelength limit, indicating that cross-sectional tessellations of $n \geq 5$ enable the homogenization approximation.

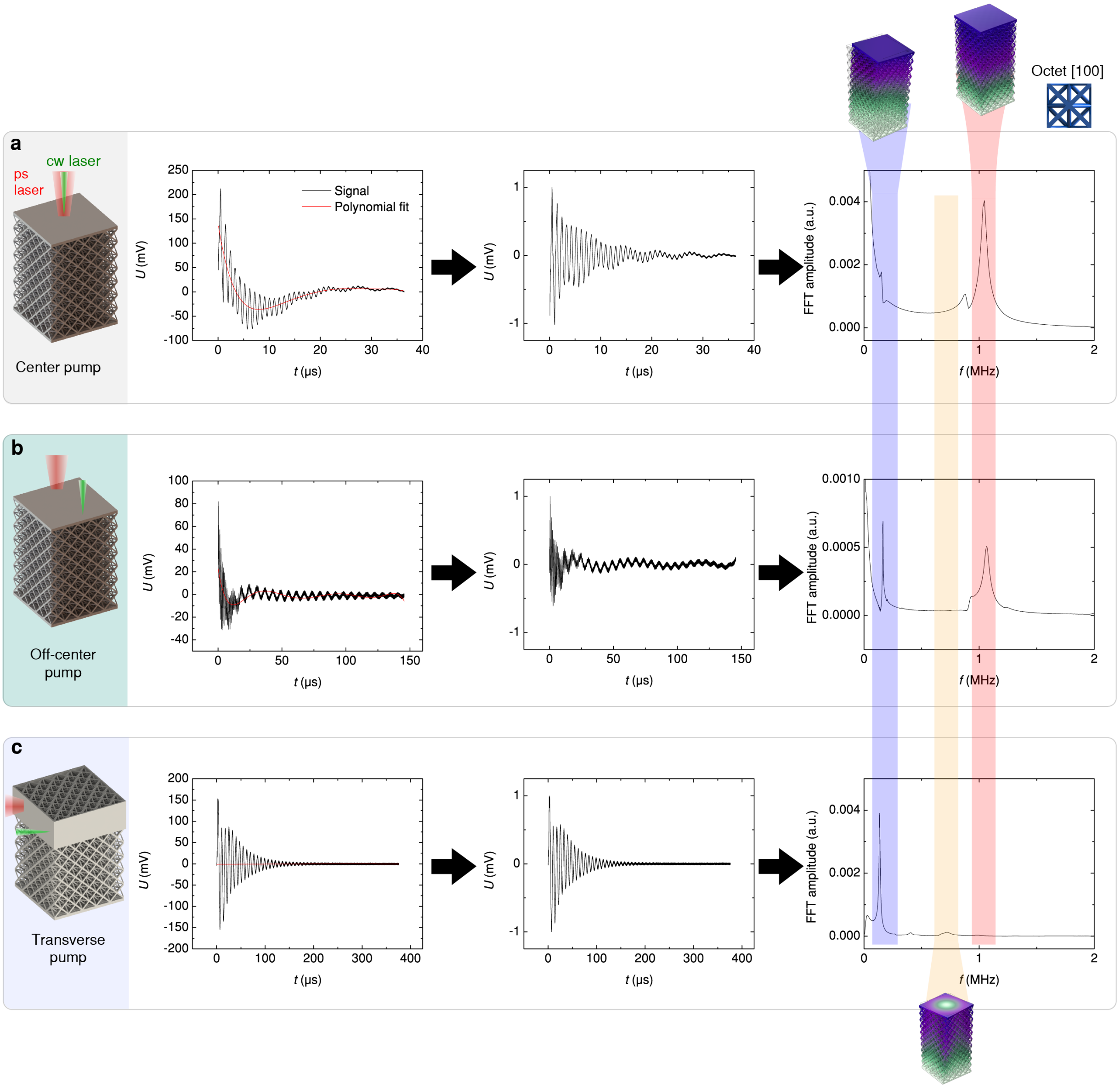

Extended Data Figure 3 | Signal processing for LIRAS measurements. For each pump scheme, photovoltage is plotted as a function of time, corresponding to the surface displacement as a function of time. The thermal background is removed by subtracting the raw data with a fifth-order polynomial fit function. Subsequently, the background-subtracted time-domain signal is converted into the frequency domain using a fast Fourier transform (FFT). Here, the signal of a $5 \times 5 \times 22$ octet in the [100] orientation is chosen for demonstration purposes.

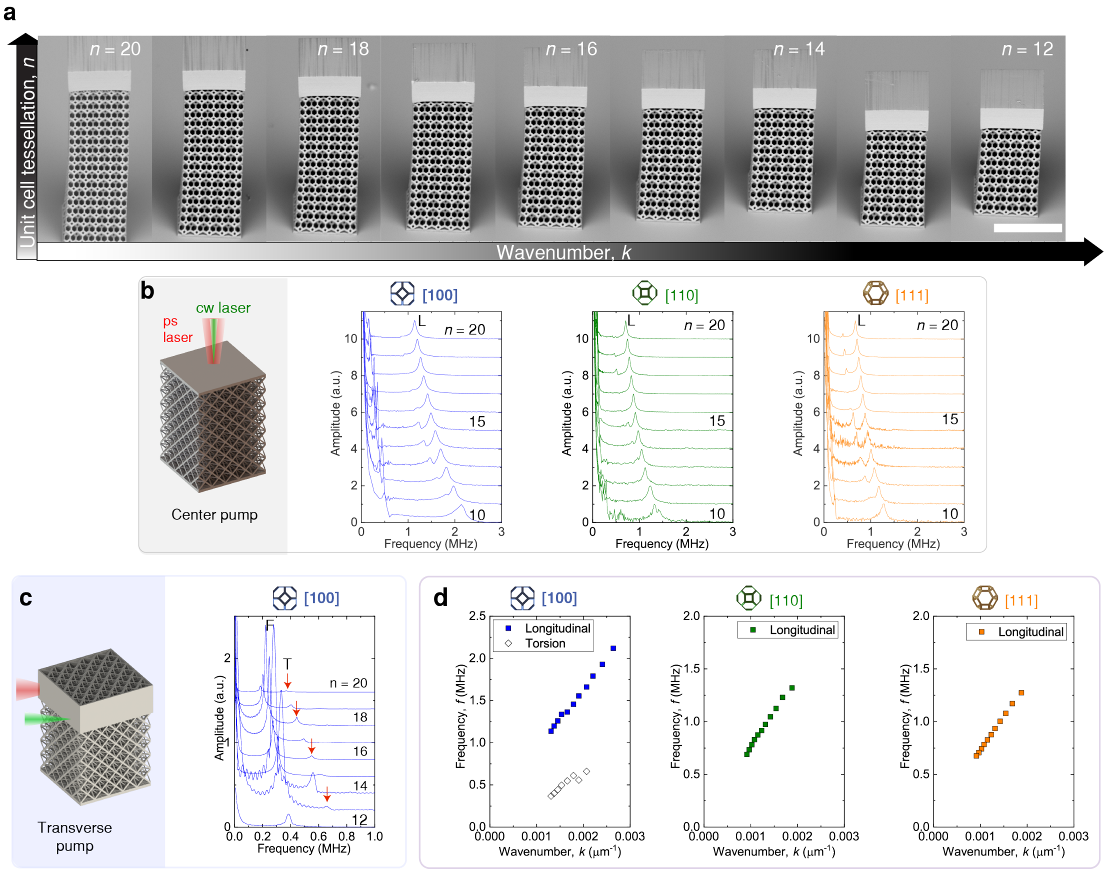

Extended Data Figure 4 │ Acoustic spectra and dispersion relations of tetrakaidecahedron samples. a, SEM images of selected [100] samples for illustration. Scale bar, 50 μm. **b**, Acoustic spectra experimentally determined using the center-pump scheme of LIRAS. **c**, Transverse-pump scheme representative data. **d**, Dispersion relations extracted from the spectra.

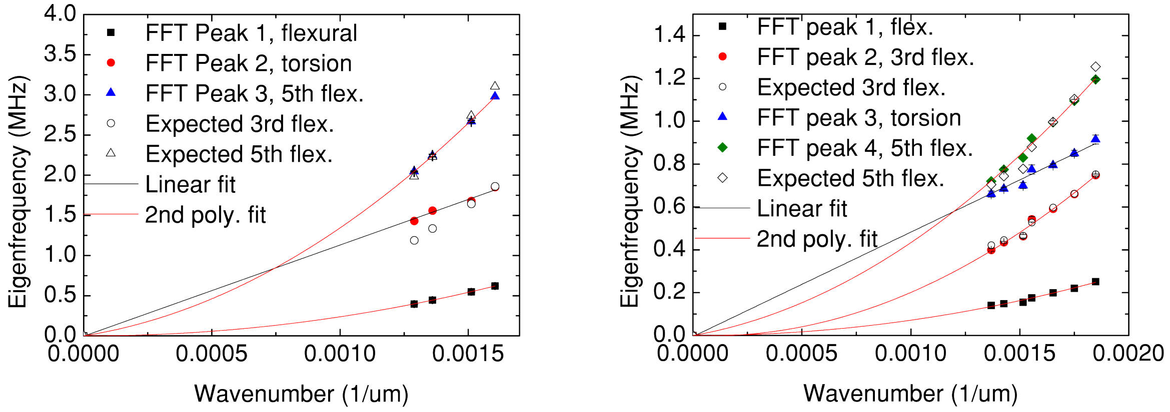

Extended Data Figure 5 | Experimental dispersion trend analysis for spectral-peak identification. Long-wavelength-limit dispersion relations extracted from Fig. 2e for monolithic IP-Dip polymer (left) and octet [100] (right) samples for a transverse-pump scheme. The spectral peaks with a nondispersive behavior (linear relation between frequency and wavenumber) correspond to the torsional modes. Following elasticity theory, longitudinal and torsional waves are nondispersive in the long-wavelength limit, while flexural waves have distinctive quadratic dispersion[46]. Furthermore, since the longitudinal mode is not activated in the transverse pump scheme, the torsional mode can be assigned to the spectral peak with a linear $f(k)$ relation. The expected 3rd and 5th-order harmonics of the flexural mode are calculated by multiplying the measured fundamental flexural frequencies by factors 3 and 5, respectively.

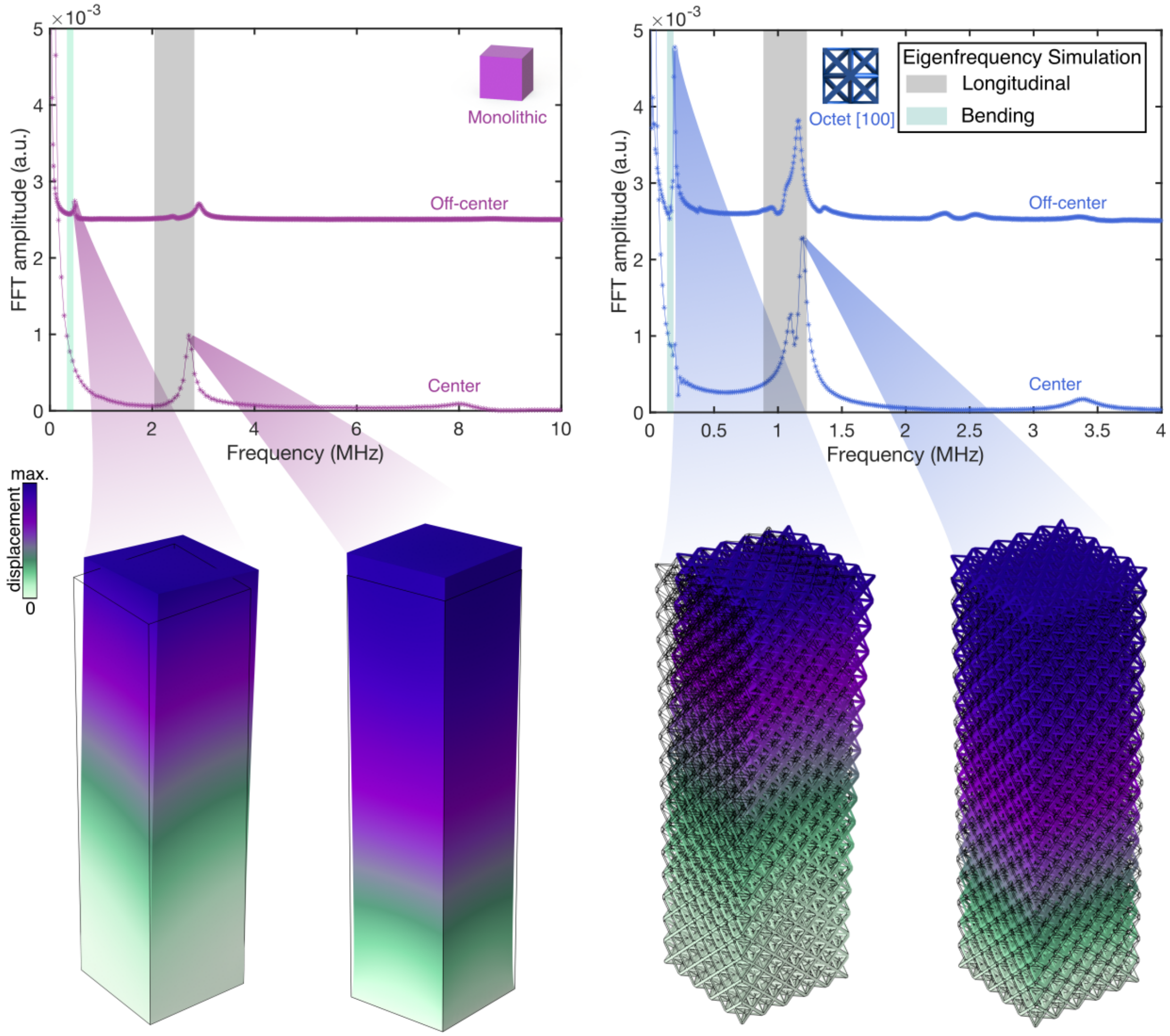

Extended Data Figure 6 | Illustration of vibrational modes corresponding to the measured acoustic spectra using FEM simulation. Shaded regions show eigenfrequency-simulation lower (quasi-static effective Young's modulus) and upper (high-strain-rate effective stiffness) bounds. Sample center-pump and off-center-pump FFTs (pictured with a DC offset for clarity) and their corresponding longitudinal and bending modes, respectively, are pictured for monolithic and octet [100] samples. Note that the torsional mode is determined in separate spectra.

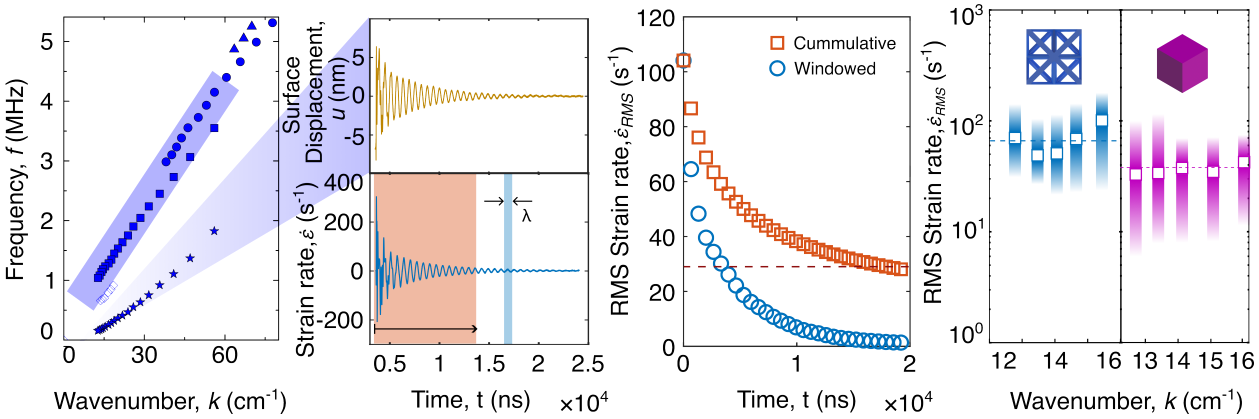

Extended Data Figure 7 | Strain rate analysis. A 5×5×20 octet sample in the [100] direction is chosen for display, demonstrating calculation of an approximate time-dependent strain rate from LIRAS measurements. From the time-displacement measurements (second panel), the strain is approximated by dividing by the sample height, while the strain rate is obtained from the time derivative of the strain-time signals (see Supplementary Information Sections III & IV). Due to the time-dependent magnitude of the strain rate, we obtain characteristic strain rates by computing the root mean square (RMS) strain rate for every wavelength (shown as windowed [blue]) as well as the cumulative RMS strain rate over multiple wavelengths up to a certain point in time (shown as cumulative [red]) in the third panel. The RMS strain rate over the entire signal is extracted as the primary characteristic strain rate for each experiment (dashed line in third panel). The RMS strain rates calculated over the first and last wavelengths are considered as the higher and lower strain-rate limits, respectively. The corresponding strain-rate range is thus presented as shaded regions in the fourth panel. The average of these values over the tallest five pillars/lattices (5-lowest wavenumber samples in the first panel) is taken as the characteristic strain rate and its limits for that structure. We selected this single value of RMS strain rate to be representative for LIRAS experiments on each structure.

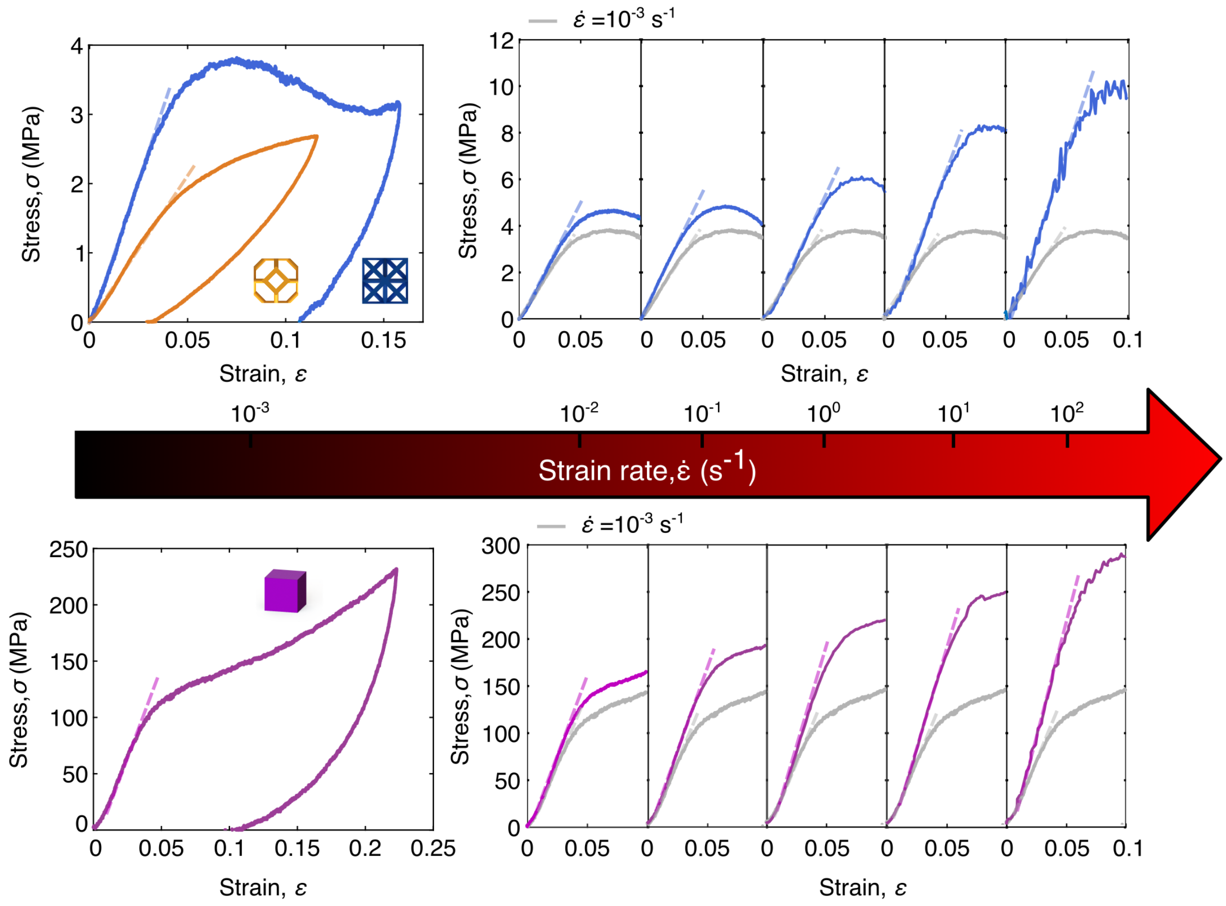

Extended Data Figure 8 | Quasi-static and dynamic uniaxial compression experiments. Quasi-static compression ($\dot{\varepsilon} = 10^{-3}$ s^{-1}) of $5 \times 5 \times 5$ octet and tetrakaidecahedron metamaterials, and monolithic pillar (left). Stress-strain plots for octet (blue) and monolithic pillar (purple) samples for strain rates from 10^{-2} s^{-1} to 10^{2} s^{-1} (right). The quasi-static response is overlaid in grey for the higher-strain-rate responses.

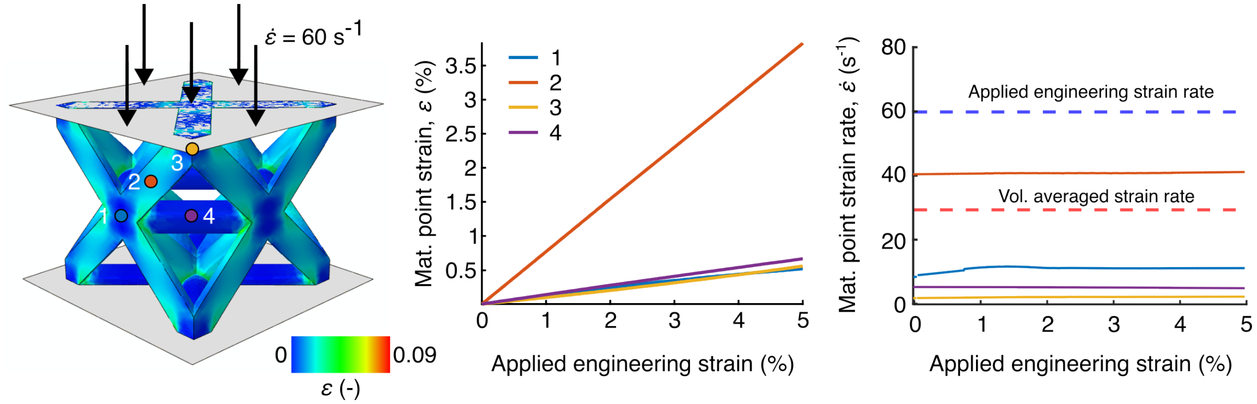

Extended Data Figure 9 | Dynamic explicit simulation of octet unit cell at 60 s^{-1} strain rate. 3D plot of the maximum absolute logarithmic strain (ε) is shown for a particular time instant when the applied engineering strain is 5%. Maximum absolute logarithmic strain and strain rate as a function of time are shown at the 4 representative material points labeled in the 3D plot (middle panel). The maximum strain rate is seen at point 2 for the given applied engineering strain rate. The volume-averaged maximum absolute logarithmic strain rate is approximated to be 48% of the applied engineering strain rate.

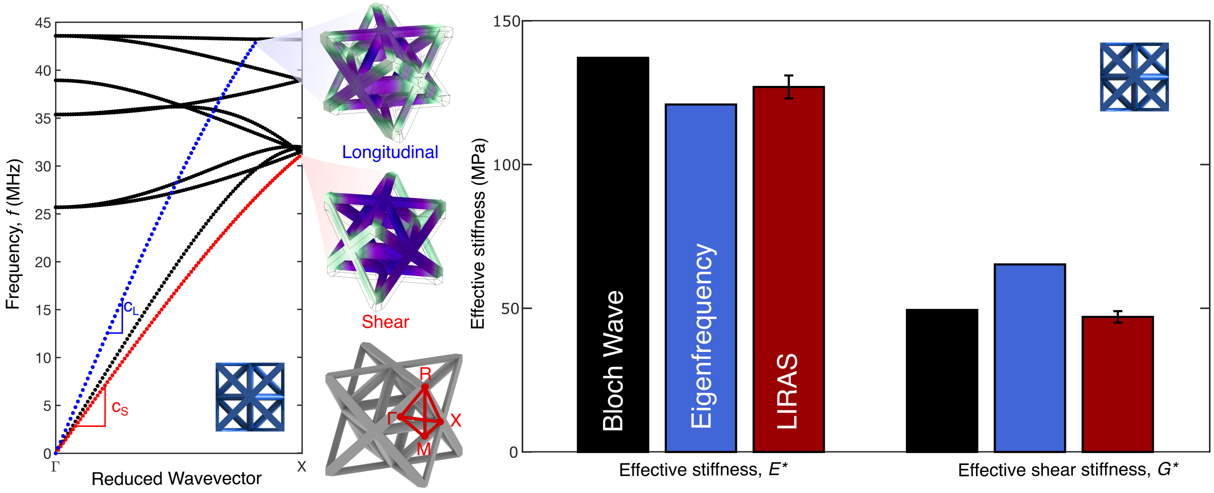

Extended Data Figure 10 | Bloch-wave velocity extraction and comparison of numerical and experimental effective stiffness and effective shear stiffness. Longitudinal and shear velocities were extracted from the slope of the linear portion of the longitudinal and shear bands of the Γ–X orientation, respectively. Transverse velocities were extracted from the linear portion of the shear band of the Γ–M orientation, but are not pictured. The bar plot depicts the difference in effective stiffness and effective shear stiffness obtained from Bloch-wave analysis[45] and eigenfrequency simulations compared to LIRAS experiments. The higher shear stiffness observed in eigenfrequency analysis might indicate that the chosen material properties are higher than in reality for this torsional mode, since the chosen material properties were matched to the strain rates of the longitudinal mode. In other words, the material-point strain rates in the torsional mode are likely lower than those for the longitudinal mode.